Korean J. Chem. Eng., 35(9), 1889-1910 (2018)
DOI: 10.1007/s11814-018-0099-4

pISSN: 0256-1115
eISSN: 1975-7220

Fabrication of composite membranes for pervaporation of tetrahydrofuran-water: Optimization of intrinsic property by response surface methodology and studies on vulcanization mechanism by density functional theory

Manas Mahapatra, Mrinmoy Karmakar, Arnab Dutta, and Nayan Ranjan Singha†

Advanced Polymer Laboratory, Department of Polymer Science and Technology,
Government College of Engineering and Leather Technology (Post-Graduate),
Maulana Abul Kalam Azad University of Technology, Salt Lake, Kolkata - 700106, West Bengal, India
(*Received 31 January 2018 • accepted 13 June 2018*)

Abstract−Response surface methodology (RSM) optimized accelerator-to-sulfur (A/S) ratio was used to synthesize semi efficiently vulcanized styrene butadiene rubber (SBRSEV0) membrane possessing optimum balance between tensile strength (TS) and elongation at break (EAB). In addition, composite membranes, such as SBRSEV8, SBRSEV12 and SBRSEV24, were fabricated via incorporating 8, 12 and 24 wt% carbon black filler (CBF), respectively. The changes in physicochemical properties, as a result of crosslinking and CBF loading, were determined by analyzing CP MAS ^{13}C-NMR, FTIR, TGA, DSC, XRD, FESEM-EDX and crosslink densities. Several bi-/poly-sulfidic products, formed by crosslinking precursors of SBR in accelerated sulfur vulcanization, were examined to ascertain the unambiguous reaction mechanism. In this regard, an extensive density functional theory (DFT) based optimization was conducted to apprehend the relative variation in stabilities of several mono-/poly-crosslinked configurations by measuring dipole moments and ground state energies. Moreover, intrinsic membrane properties, such as partial permeabilities and diffusion coefficients, were measured at varying conditions. RSM was employed to optimize membrane efficiency resulting from individual and/or interactive effects of input variables. For the first time, systematic three-stage RSM based optimization (i.e., TS/EAB, total flux (TF)/separation factor (SF) and partial permeabilities) was used to ensure excellent balance between TS/EAB (5.78 MPa/499.008% at 2.32 and 3.29 wt% of A and S, respectively), minimum TF/maximum SF (36.90 g m^{-2} h^{-1}/202.46 at 35 °C, 0.97 wt% tetrahydrofuran (THF) and 24 wt% CBF) and minimum/maximum partial permeabilities of water/THF (2.94×10^{-8}/4.64×10^{-8} Barrer at 35 °C, 0.97 wt% THF and 11.49 wt% CBF).

Keywords: Filled and/or Crosslinked Organoselective Styrene Butadiene Rubber Membrane, Optimization of Sulfur-accelerator-filler of Composite Membrane by RSM, CP MAS ^{13}C NMR, FTIR, TGA, DSC, XRD, FESEM, EDX and Crosslink Density Analyses, Permeability, Diffusion Coefficient, Activity Coefficient and Solubility Parameter of Synthetic Rubber Membrane, Analysis of Vulcanization Mechanism by DFT, Organic-water Separation

INTRODUCTION

Styrene butadiene rubber (SBR), a copolymer of styrene and butadiene, is extensively used in making shoe heels/soles, car tyres, gaskets, chewing gum and as sealing and binding agents for walls, floors and roofs. The heterocyclic colorless THF possesses adequate water solubility, potential basicity, low viscosity, high dielectric constant (7.6) and dipole moment (1.63 D) [1]. THF is commonly employed as an expensive solvent for dissolving several monomers/polymers, in hydroboration and Grignard reactions, liquid chromatography along with manufacturing colors, glues, color toners and therapeutic products. Therefore, waste effluents of several industries contain dissolved THF. However, THF is highly inflammable and imparts severe health hazards to human beings, such as headache, nausea and dizziness. Exposure to high concentration of THF can damage liver and kidneys as well as irritate and burn skin and eyes severely, leading to permanent damage. Moreover, THF vapor can irritate nose, throat and lungs to symptomize cough, wheezing and shortness of breath. Thus, recycling and reuse of THF is essential. THF-water mixture, containing 94.3 wt% THF, forms an azeotrope at 63.9 °C and thus, limits the separation by conventional distillation process. Furthermore, this process may lead to explosion due to the formation of unstable peroxides when THF comes in contact with oxygen [2].

Membrane based separation technologies play pivotal role and are of paramount importance for purification, concentration and fractionation of fluid mixtures as well as for efficient removal of dissolved impurities from industrial effluents by the prevalent alleviated selectivity, lower energy consumption, higher performance-to-cost ratio and compact modular design [3,4]. Pervaporation, a membrane based technique, is extensively used for dehydration, separation of volatile organic compounds, azeotropes and close boiling liquids [1-9]. Meanwhile, the use of hydrophilic membranes for dehydration from THF-water mixtures has already been reported, whereas the reverse has rarely been performed due to the lack of physicochemically stable organoselective membranes [10]. In fact,

†To whom correspondence should be addressed.
E-mail: drs.nrs@gmail.com

the amorphous nature of most of the elastomers restricts their utilization as organophilic membranes. Indeed, an optimum level of vulcanization introduces good balance between TS and EAB as a result of the enhanced elasticity.

Although several works have been devoted to elucidate the interaction between rubber chains and vulcanizing agents [9], the unambiguous attainment of vulcanization mechanism via formation of poly-sulfidic crosslinks by H-abstraction, radical addition, radical coupling and sulfur-transfer is yet to be reported. In the present study, the mechanisms of vulcanization were established via analyzing CP MAS ^{13}C-NMR, FTIR and extensive DFT. In fact, the energies and dipole moments of different crosslinked networks produced during sulfur vulcanization of SBR were attempted for the first time by DFT to identify the lowest energy configuration.

Pervaporation is a conventional method of separation, in which the effect of only one parameter on response can be monitored at a time while keeping the others constant. This requires enormous experimental runs and is unable to predict the interactive effects of the operating parameters on responses. In RSM, all the independent factors are varied simultaneously for optimization of process variables to evaluate the relative significance of the influencing factors, even in the presence of complex interactions. Meanwhile, few works on pervaporation of organics (other than THF separation) using rubber membranes, such as NR, SBR, EPDM and PDMS, have been devoted for RSM based performance optimization [11-17]. Most of these reported works were carried out by assuming only the individual effects of input variables (e.g., accelerator or sulfur for property and temperature, feed concentration and filler for performance) on responses (e.g., TS/EAB and TF/SF). However, no attempts have been made till date to account for the synergistic effects of these variables on responses of composite rubber membranes and their effects on membrane intrinsic properties, such as PPs and DCs, which more realistically consider sorption, diffusion and permeation, simultaneously, and rather more important parameters for reporting the pervaporation processes. In fact, the multi-stage RSM based optimization in pervaporation of THF-water, using CBF filled and crosslinked SBR membranes, has not yet been reported. As membrane properties are found to vary significantly even after the small changes in either A/S or wt% of filler, prevalence of the optimum physicochemical properties can be possible only by the incorporation of optimum amounts of filler, accelerator and sulfur, obtained by RSM. Although few attempts have been made to attain the optimum balance of aforesaid properties by gradual addition of ingredients in different amounts to avoid the appearance of either very high crosslink densities or formation of filler aggregates, successive three-stage optimization of A/S ratio for obtaining optimum balance between TS and EAB, followed by operational variables, such as TF and SF, and finally, intrinsic membrane properties, such as partial permeabilities of THF and water, in separation of THF-water, and extensive characterization of membranes via spectroscopic (CP MAS ^{13}C-NMR, FTIR and EDX), thermal (TGA, DSC), diffractometric (XRD), microscopic (FESEM), computational (DFT) and mechanical (crosslink densities) method have been reported for the first time. An unorthodox three-stage RSM has rationally been incorporated for optimizing synthesis/property and performance parameters via performing the minimum number of experimental runs. In fact, such synthesis-property-performance optimization of rubber membranes in a single study is yet to be reported.

THEORY

1. Sorption Thermodynamics

Sorption of THF (1) and water (2) was determined from the measurements of interaction parameters between solvents in feed (χ_{12}^{f}) and membrane (χ_{12}^{m}). Again, χ_{12}^{f} is estimated using Eq. (1a) based on Flory-Huggins thermodynamics [9].

$$\chi_{12}^{f}=\frac{1}{x_1v_2}\left[x_1\ln\left(\frac{x_1}{v_1}\right)+x_2\ln\left(\frac{x_2}{v_2}\right)+(x_1\ln\gamma_1+x_2\ln\gamma_2)\right] \tag{1a}$$

Here, v_1/x_1 and v_2/x_2 are volume fractions/mole fractions of 1 and 2 in feed mixture, respectively. Indeed, interaction parameters of 1 and 2 in membrane and feed are obtained from volume fractions of components, using a method reported elsewhere [9]. In addition, the interaction parameter between solvent (1) and membrane (χ_{1p}) is obtained from volume fraction of polymeric membrane (j_p) using Eq. (1b).

$$\chi_{1p}=\frac{-\ln(1-\varphi_p)-\varphi_p}{\varphi_p^2} \tag{1b}$$

Activity coefficients of 1 and 2 at different feed compositions are determined using Wilson Eq. (2a) and (2b).

$$\ln\gamma_1=-\ln(x_1+\Lambda_{12}x_2)+x_2\left(\frac{\Lambda_{12}}{x_1+\Lambda_{12}x_2}-\frac{\Lambda_{21}}{x_2+\Lambda_{21}x_1}\right) \tag{2a}$$

$$\ln\gamma_2=-\ln(x_2+\Lambda_{21}x_1)-x_1\left(\frac{\Lambda_{12}}{x_1+\Lambda_{12}x_2}-\frac{\Lambda_{21}}{x_2+\Lambda_{21}x_1}\right) \tag{2b}$$

The Wilson parameters Λ_{12} and Λ_{21} for 1 and 2, respectively, are obtained from the vapor-liquid-equilibrium data [9]. In addition, solubility parameters of various solvents and polymers are obtained from literature, whereas solubility parameters of membranes (δ_p) are obtained from interaction parameters using Eq. (3).

$$\chi_{1p}=0.35+\frac{V_1}{RT}(\delta_1-\delta_p)^2 \tag{3}$$

Here, V_1 is molar volume and δ_1 is solubility parameter of 1. However, the membrane phase activity of 1 (a_1) for binary sorption is obtained using Eq. (4) [9].

$$\ln a_1=\ln(1-\varphi_p)+\varphi_p+\chi_{1p}\varphi_p^2 \tag{4}$$

If the density of membrane remains constant, mole fraction is substituted by volume fraction. Accordingly, activity of 1 within the membrane may be determined from Eq. (5a) [9].

$$a_1^m=\varphi_1^m\gamma_1^m \tag{5a}$$

Here, φ_1^m is volume fraction of 1 within the membrane. However, for a single component sorption by membrane, $a_1^m=1$ and thus, activity coefficient of a single component in membrane (state-I) is calculated using Eq. (5b).

$$\gamma_1^m=\frac{1}{\varphi_1^m} \tag{5b}$$

Again, state-II accounts for the coupling of each component with

membrane, avoiding self-interaction effects between 1 and 2, and is calculated using Eq. (5c).

$$\ln\gamma_1^m = \varphi_p + \chi_{1p}\varphi_p^2 = (1-\varphi_1) + \chi_{1p}(1-\varphi_1)^2 \tag{5c}$$

In succession, activity coefficients of 1 and 2 (state-III) are obtained using Eq. (5d) and (5e) [9], assuming the prevalent coupling effect of the components.

$$\ln\gamma_1^m = \varphi_p + \chi_{1p}\varphi_p^2 + \left(1-\frac{V_1}{V_2}\right)\varphi_2 + \chi_{12}\varphi_2^2 + \left(\chi_{12}+\chi_{1p}-\frac{V_1}{V_2}\chi_{2p}\right)\varphi_2\varphi_p - u_1u_2\varphi_2\frac{\delta\chi_{12}}{\delta u_2} \tag{5d}$$

$$\ln\gamma_2^m = \varphi_p + \chi_{2p}\varphi_p^2 + \left(1-\frac{V_2}{V_1}\right)\varphi_1 + \frac{V_2}{V_1}\chi_{12}\varphi_1^2 + \frac{V_2}{V_1}\left(\chi_{12}-\chi_{1p}+\frac{V_1}{V_2}\chi_{2p}\right)\varphi_1\varphi_p + \frac{V_2}{V_1}u_1^2\varphi_2\frac{\delta\chi_{12}}{\delta u_2} \tag{5e}$$

Here, u_1 and u_2, volume fractions of 1 and 2, respectively, are determined from Eq. (5f) and (5g).

$$u_1 = \frac{\varphi_1}{\varphi_1+\varphi_2} \tag{5f}$$

and

$$u_2 = \frac{\varphi_2}{\varphi_1+\varphi_2} \tag{5g}$$

2. Permeability

According to the solution diffusion model, mass flux of 1 is related to the vapor pressure difference between feed and permeate sides (Eq. (6)).

$$J_1 = \frac{P_1}{l}(p_f - p_p) \tag{6}$$

Here, l, p_f, p_p and P_1 are membrane thickness, feed and permeate side vapor pressures of 1 and intrinsic membrane permeability, respectively. However, P_1/l is termed as membrane permeance [9]. The vapor pressure of 1 on feed side (p_f), i.e., fugacity (f_1), is obtained using Eq. (7).

$$p_f = x_1\gamma_1 p_s = f_1 \tag{7}$$

Here, p_s, x_1 and γ_1 are saturated vapour pressure, mole fraction and activity coefficient of 1 on feed side, respectively. The extreme low pressure in the permeate side is sufficient to consider the ideal state of permeants. Thus, partial vapor pressure of 1 on permeate side (p_p) may be obtained [1] using Eq. (8).

$$p_p = y_1 P_p \tag{8}$$

Here, P_p is total permeate pressure and y_1 is mole fraction of 1 on permeate side and, consequently, Eq. (6) may be rewritten as Eq. (9a) [18].

$$J_1 = \frac{P_1}{l}(x_1\gamma_1 p_2 - y_1 P_p) \tag{9}$$

or, $$P_1 = \frac{J_1 l}{(f_1 - y_1 P_p)} \tag{9a}$$

Here, saturated vapor pressures of 1 and 2 may be calculated using Antoine equation. As vapor pressure of permeate side is too low, Eq. (9a) may be modified to Eq. (9b).

$$P_1 = \frac{J_1 l}{f_1} \tag{9b}$$

3. Diffusion Coefficient

Diffusion of permeants through dense membrane is more accurately expressed in terms of solvent volume fraction. As the per transfer solution volume fraction model, the ratio of partial flux of components 1 and 2 through a membrane is expressed using Eq. (10) [19].

$$\frac{J_1}{J_2} = \frac{D_{10}V_2}{D_{20}V_1}\frac{d\varphi_1}{d\varphi_2} \tag{10}$$

Here, J_1, D_{10}, V_1 and φ_1 are partial flux, diffusion coefficient at infinite dilution, molar volume and membrane phase volume fraction of 1, respectively. Integration of Eq. (10) from upstream to downstream side of membrane results in Eq. (11).

$$\frac{J_1}{J_2} = \frac{D_{10}V_2}{D_{20}V_1}\frac{\varphi_{1u}-\varphi_{1d}}{\varphi_{2u}-\varphi_{2d}} \tag{11}$$

However, the concentration on the downstream side is too low to be considered and hence, $\varphi_{1d}=\varphi_{2d}=0$. Thus, Eq. (11) reduces to Eq. (12).

$$\frac{J_1}{J_2} = \frac{D_{10}V_2}{D_{20}V_1}\frac{\varphi_{1u}}{\varphi_{2u}} \tag{12}$$

From flux, molar volume and membrane phase upstream side volume fractions of 1 and 2, D_{10} and D_{20} are obtained.

Furthermore, partial flux of component 1 is expressed by Eq. (13).

$$J_1 = \frac{D_{10}}{V_1 L}\frac{\varphi_{1u}-\varphi_{1d}}{\varphi_{2u}-\varphi_{2d}}\int_{\varphi_d}^{\varphi_u}\gamma\varphi_1 d\varphi_1 \tag{13}$$

or, $$J_1 = \frac{D_{1m}}{V_1 L}(\varphi_{1u}-\varphi_{1d}) \tag{14}$$

Here, L is membrane thickness and $D_{1m} = \frac{D_{10}}{\varphi_u-\varphi_d}\int_{\varphi_d}^{\varphi_u}\gamma\varphi_1 d\varphi_1$

or, $$D_{1m} = D_{10}\frac{e^{\gamma\varphi_u}-e^{\gamma\varphi_d}}{\gamma(\varphi_u-\varphi_d)} \tag{15}$$

Thus, $$J_1 = \frac{D_{10}(e^{\gamma\varphi_u}-e^{\gamma\varphi_d})}{V_1 L\,\gamma(\varphi_u-\varphi_d)}(\varphi_{1u}-\varphi_{1d}) \tag{16}$$

For low downstream pressure, $\varphi_d=0$ and $e^{\gamma\varphi_d}=1$.

Therefore, $$J_1 = \frac{D_{10}}{\gamma V_1 L}\frac{e^{\gamma\varphi_u}-1}{1+\varphi_{2u}/\varphi_{1u}} \tag{17}$$

Here, φ_u (i.e., $\varphi_{1u}+\varphi_{2u}$) represents the total solution volume fraction on upstream side of membrane. The plot of partial flux with total sorbed volume fraction (φ_u) gives a regressed exponential equation with fairly good fitting of experimental data.

EXPERIMENTAL

1. Materials

SBR was obtained from TCI, West Bengal, India. CBF was sup-

Table 1. Characterization of membranes

Sr. No.	Characterization technique	Model/make	Operational conditions
i.	FTIR	Spectrum-2, Singapore	Performed using a thin film within 4,000-400 cm^{-1}
ii.	CP MAS ^{13}C-NMR	JEOL ECX400	Performed at a frequency of 100 MHz
iii.	TGA	Pyris 6 TGA, The Netherlands	Operated in N_2 atmosphere with flow and scanning rates of 20.0 cm^3 min^{-1} and 10 °C min^{-1}, respectively, within 30-700 °C
iv.	DSC	Pyris 6 DSC, The Netherlands	Operated in N_2 atmosphere with flow rate of 20.0 cm^3 min^{-1} within 30-442 °C
v.	XRD	X'Pert PRO, made by PANalytical B.V., The Netherlands using Ni-filtered Cu K_α radiation (λ=1.5418 Å)	Operated at the scanning rate of 2θ=0.005° s^{-1} and angle of diffraction from 2 to 72°
vi.	FESEM and EDX	ZEISS EVO-MA 10 having resolution of 3 nm with W filament and Sb as sources	2.9 kV and 10 K magnification

plied by PCBL (West Bengal, India). Zinc diethyldithiocarbamate (ZDC), sulfur, stearic acid and THF were purchased from Merck Specialties Private Ltd., India.

2. Fabrication of Pervaporation Membranes

SBR was masticated and then swelled in toluene for 24 h, followed by adding 8, 12 and 24 wt% of CBF with mechanical stirring to obtain homogeneous dispersions. In succession, sulfur and ZDC of 2.32 and 3.29 wt% of SBR, respectively, were added with constant stirring for another 8 h. The as-prepared rubber dispersion was then cast on glass plate and air dried overnight at ambient conditions, followed by crosslinking in a furnace at 110 °C for 1 h. These cured membranes were then cooled by submerging glass plates in cold water, followed by peeling out the membranes. The average thickness of the membranes was 50±0.55 μm.

3. Characterization of Membranes

SBRSEV membranes were characterized using the techniques as described in Table 1.

In addition, SBRSEV membranes were also characterized by measuring TS, EAB and modulus by Lloyd-UTM, England as per ASTM D 882-97 for polymeric film and crosslink densities by chemical and mechanical methods. Image analyses on FESEM photomicrographs and RSM were conducted by ImageJ, NIH, USA and Design Expert 7.0.0 software, respectively.

4. Sorption Study

The known weight, 1 g, of thick membranes was immersed in 25 cm^3 of different known concentrations of THF-water mixtures and allowed to equilibrate for 96 h at 35 °C. These membranes were then taken out from solutions periodically and weighed after wiping out the superfluous liquid until the attainment of constant weight. Indeed, the increase in weight was equal to the total amount of THF and water sorbed by the membranes. After measuring the total weight of sorbed membranes from above experiment, thick samples, collected in a 250 cm^3 conical flask, were kept in a constant temperature bath, and connected to a cold trap and vacuum pump in series (Scheme 1(a)). The cold trap was immersed in liquid N_2 flask. The sorbed membrane was then forced to desorp under vacuum and the vapour coming out was freezed and collected in the cold trap immersed in liquid N_2. The amount of THF, sorbed by membranes, was estimated by the compositional analysis of the liquefied vapor using Abbe type refractometer (Abbemat-HP, Anton Paar, Austria) at 30 °C. From the weight of total sorption and corresponding THF content in the membrane, sorption selectivity ($\alpha_{s(1)}$) of the membrane for 1 was calculated using Eq. (18) [20].

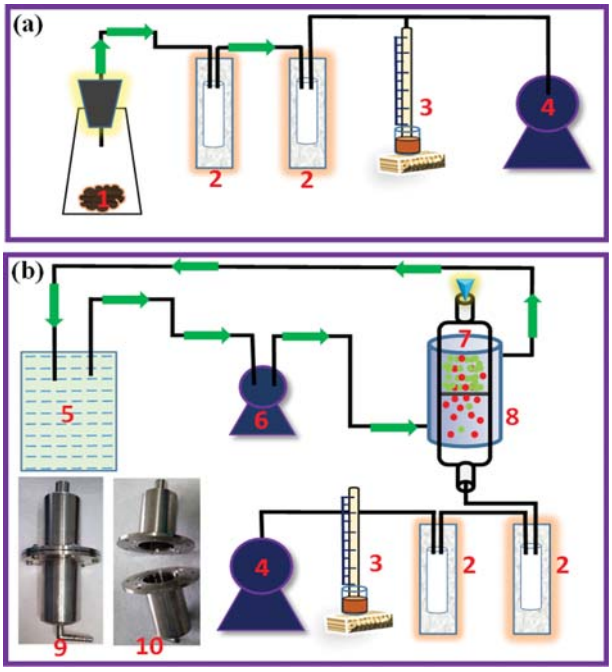

Scheme 1. (a) Experimental setup for sorption and (b) pervaporation.

1. Sorbed membrane
2. Liquid N_2 trap
3. Hg manometer
4. Vacuum pump
5. Hot water bath
6. Water circulating pump
7. Pervaporation cell
8. Hot water circulating jacket
9. Photograph of pervaporation cell
10. Photograph of male (above) and female (below) portion of pervaporation cell

$$\alpha_{s(1)} = \frac{y_{m1}/y_{m2}}{x_{f1}/x_{f2}} \quad (18)$$

Here, y_{m1} and x_{f1} represent concentrations of 1 in membrane and feed, respectively.

5. Pervaporation Study

The downstream pressure in pervaporation experiments was measured using a Hg manometer (Scheme 1(b)) [21]. The feed section of pervaporation cell was fitted to stirrer and thermometer for avoiding concentration and temperature gradients, respectively, while effective membrane area (A′) and volume of the feed compartment were 19.6 cm^2 and 150.0 cm^3, respectively. The THF-water feed mixture was allowed to equilibrate for 3 h in contact with the membrane for the first experiment, followed by 1.5 h for the subsequent experiments. In this context, permeation flux (J), defined as the ratio of the amount of total permeates (W) to the product of area of membrane (A′) and experimental time (t), was obtained using Eq. (19) [22].

$$J=\frac{W}{A't} \tag{19}$$

The isothermal condition of pervaporation experiment was maintained by circulating fixed temperature water around the jacket of pervaporation cell. THF content of permeate was determined by Abbe type digital Refractometer at 30 °C. Permeation selectivity or SF of THF (α_1) of membranes was evaluated using Eq. (20).

$$\alpha_1=\frac{y_1/y_2}{x_1/x_2} \tag{20}$$

Here, y_1 and x_1 are weight fractions of 1 in permeate and feed, respectively.

RESULTS AND DISCUSSION

1. FTIR Analysis

As shown in Fig. 1(a), with respect to SBR, numerous newly arrived characteristic peaks for SBRSEV0 within 700-600 and 500-400 cm^{-1} indicated the formation of C-S-C/C-S and S-S bonds in SBRSEV0, respectively (Table 2). In this context, SBRSEV0 showed

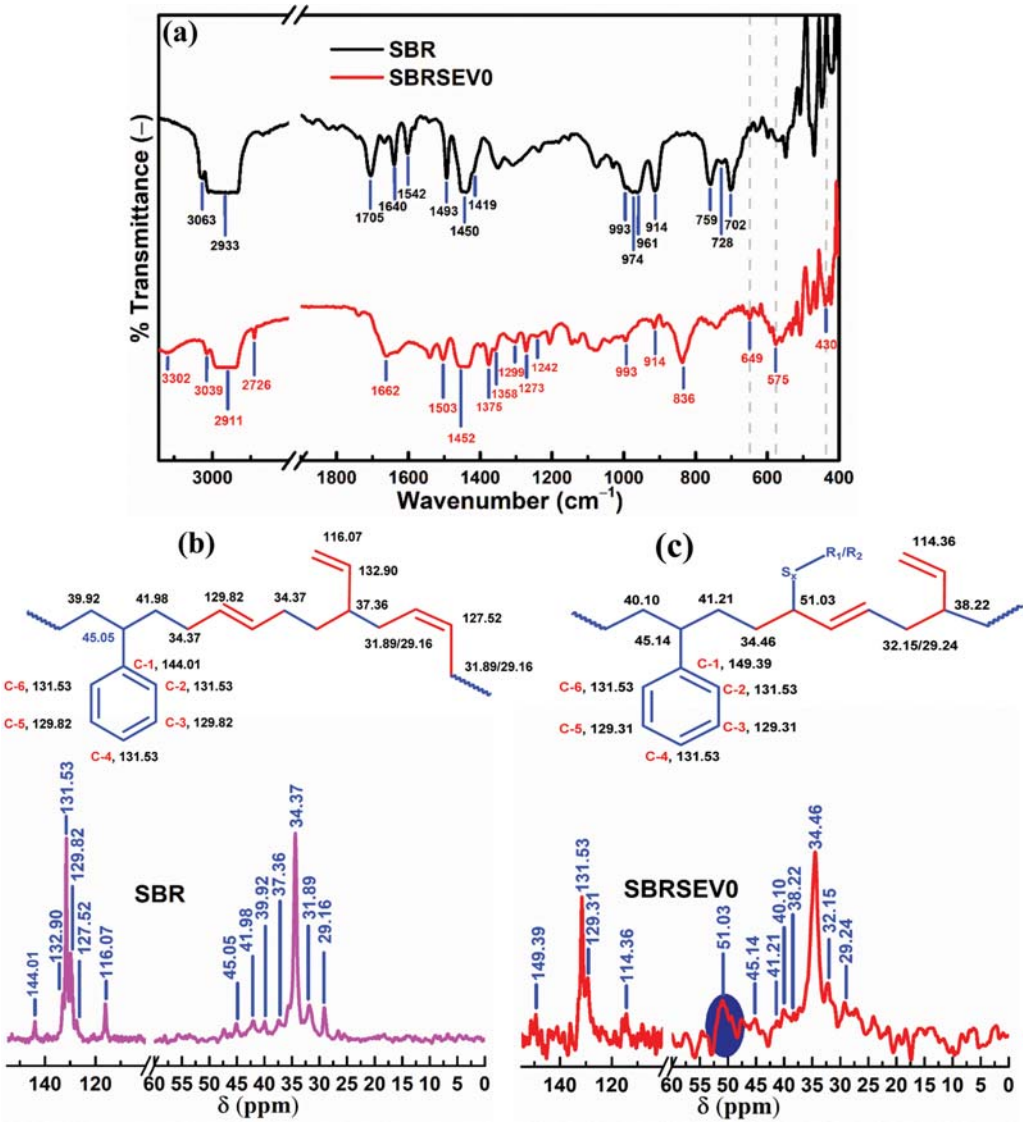

Fig. 1. (a) FTIR and (b/c) CP MAS ^{13}C NMR of SBR/SBRSEV0.

Table 2. FTIR analyses of SBR and SBRSEV0

Wavenumber (cm^{-1})		Assignment of peaks
SBR	SBRSEV0	
Absent	430	S-S *str.* of vulcanized membrane [9]
Absent	500-400	S-S *str.* of vulcanized membrane
Absent	575/649	C-S *str.* of vulcanized membrane [9]
Absent	700-600	C-S-C/C-S *str.* of vulcanized membrane
702	Absent	Out of plane C-C *bending* of styrene moiety in SBRSEV0 [29]
728	Absent	Conversion of -CH_2- to >CH- of C-H *bending* of butadiene [26]
759	Absent	Out of plane C-H *bending* [31]
Absent	836	Out of plane C-H *def.*
914	914	1,2-Butadiene or vinyl-butadiene moiety [23]
961/974	Absent	C-H *str.* of -CH_2-, attached to -CH=CH-, that converted to >CH- [25]
993	993	Out of plane vinylic C-H *bending* [28]
Absent	1299/1242	-CH_2- *wagging* of 1-3-monolayer films of *cis*-stearic acid
Absent	1273/1299	-CH_2- *wagging* in -CH_2-S- [23]
Absent	1358/1375	-CH_3 moiety of ethyl group in ZDC [29]
1419/1542	Absent	ν_s(-COO^-)/ν_{as}(-COO^-) of salt of fatty acid impurities in SBR
1450	1452	Skeletal C=C vibration [30]
1493	1503	Aromatic C=C *str.*
1640	1662	C=C *str.* of backbone
1705	Absent	O=C *str.* of cyclic H-bonded -COOH dimer fatty acid impurities in SBR
Absent	2726	ν_{as}(-CHMe) due to conversion of -CH_2- into >CH- of butadiene in SBRSEV0 [27]
2933	2911	Significant shifting in C-H *str.* due to transformation of -CH_2- to >CH- [24]
3063	3032	C-H *str.* of aromatic ring
3063	3039	Change in aromatic environment due to vulcanization
Absent	3302	Mutual H-bonding between O-H and N-H of ZDC [32]

distinct peaks at 649/575 and 430 cm^{-1} for C-S and S-S linkages, respectively [9]. Consequently, the change in -CH_2- *wagging* in -CH_2-S- was also reflected in the arrival of peaks at 1,273 and 1,299 cm^{-1} in SBRSEV0 [23]. Accordingly, the prevalent sulfur crosslinking between rubber moieties, associated with transformation of -CH_2- to >CH- groups, led to the substantial shifting of C-H *str.* from 2,933 to 2,911 cm^{-1} [24]. In fact, the vulcanization driven transformation of -CH=CH- linked -CH_2- into >CH- for butadiene unit of backbone was demonstrated by the disappearance of broad peaks at 961 and 974 cm^{-1} in SBRSEV0, respectively [25]. Moreover, the disappearance of C-H *bending* peak at 728 cm^{-1} of butadiene was ascribed to the conversion of -CH_2- to >CH- of butadiene in SBRSEV0 [26], which was also supported by the newly generated peak at 2,726 cm^{-1}, ascribed to the ν_{as}(-CHMe) of SBRSEV0 [27]. Consequently, the strong, broad and out of plane C-H *def.* band of SBRSEV0 appeared at 836 cm^{-1} with 34 cm^{-1} wide at half height. The modified nature of peak at 993 cm^{-1} was attributed to different out of plane *bending* vibrations of vinylic C-H in SBR and SBRSEV0 [28]. Nevertheless, the peak at 914 cm^{-1} could be attributed to the presence of the 1,2-butadiene or vinyl-butadiene moiety in the network of both SBR and SBRSEV0 [23], though the respective peak intensity was significantly reduced in SBRSEV0, which might be related to at least partial involvement of 1,2-butadiene or vinyl-butadiene moieties in vulcanization process. In addition, relative transformation of intense peak at 702 cm^{-1} for styrene moiety of SBR in SBRSEV0 indicated the extensive structural alterations in SBR [29]. In this regard, the shifting of peak from 3,063 to 3,039 cm^{-1} was correlated to the change in aromatic environment due to vulcanization. In addition, the change in skeletal vibration of C=C around SBR side chains due to vulcanization was reflected by the relative broadening of C=C from 1,450 cm^{-1} of SBR to 1,452 cm^{-1} in SBRSEV0 [30]. The overlapping of symmetrical and unsymmetrical C-H *str.* vibration resulted in an extremely broad spectrum. Indeed, the characteristic C-H *str.* peaks of aromatic ring in SBR and SBRSEV0 appeared as shoulders at 3,063 and 3,039 cm^{-1}, respectively. However, such peaks appeared at slightly higher frequency than C-H band of alkane. Extensive conjugation in aromatic ring resulted in the decrease in double bond strength and thus, aromatic C=C *str.* appeared at significantly lower frequency (1,493/1,503 cm^{-1} for SBR/SBRSEV0) than C=C *str.* (1,640/1,662 cm^{-1}). Additionally, out of plane *bending* vibrations of aromatic C-H and C-C bond of SBR also appeared at 759 and 702 cm^{-1}, respectively (Table 2) [31]. The chemical modification of SBR in SBRSEV0 could be apprehended by the appearance of characteristic peaks at 1,375 and 1,358 cm^{-1}, assigned to -CH_3 moiety of ethyl groups in ZDC [29]. Meanwhile, the appearance of a new peak at 3,302 cm^{-1} was attributed to the formation of mutual H-bonding between O-H and N-H of ZDC [32]. In fact, the presence of the peak at 1,705 cm^{-1} in SBR could be attributed to the O=C *str.* of cyclic H-bonded -COOH dimer, indicating the possible presence of salts of fatty acids

Table 3. CP MAS ^{13}C NMR analyses of SBR and SBRSEV0

Chemical shift (ppm)		Assignment of peaks
SBR	SBRSEV0	
31.89/29.16	32.15/29.24	-**C**H=**C**H- (*cis*)
34.37	34.46	-$\mathbf{C}H_2$- adjacent to -CH=CH- (*trans*)
37.36	38.22	>**C**H- adjacent to CH_2=CH-
39.92	40.10	$\mathbf{C}_\alpha$-CH_2 of styrene
41.98	41.21	-$\mathbf{C}H_2$- of styrene
45.05	45.14	>**C**H- of styrene
Absent	51.03	**C**-S crosslinking [33]
116.07	Absent	Vinylic $\mathbf{C}H_2$=CH-
127.52	Absent	-**C**H=**C**H- (*cis*)
129.82	129.31	**C**-3/**C**-5 of styrene units of SBR [33]/-CH=CH- (*trans*) of butadiene
131.53	131.53	**C**-2/**C**-4/**C**-6 of styrene units of SBR [33]
132.90	Absent	Vinylic CH_2=**C**H-
144.01	149.39	**C**-1 of styrene units of SBR [33]

as impurities, substantiated by the occurrence of both ν_s(-COO^-) and ν_{as}(-COO^-) in SBR at 1,419 and 1,542 cm^{-1}, respectively. However, the arrival of peaks at 1,299 and 1,242 cm^{-1} in SBRSEV0 was associated with -CH_2- *wagging* of 1-3-monolayer films of *cis*-stearic acid.

2. CP MAS ^{13}C NMR Analysis

From the analyses of high-resolution solid state CP MAS ^{13}C NMR spectra (Fig. (1b) and (c)), several structural alterations in SBRSEV0 as compared to that of SBR were inferred (Table 3). The appearance of characteristic peaks at 144.01, 131.53 and 129.82 ppm for the **C**-1, **C**-2/**C**-4/**C**-6 and **C**-3/**C**-5 was ascribed to the styrene units of SBR [33]. Moreover, peaks at 45.05, 41.98 and 39.92 ppm appeared due to >**C**H-, -$\mathbf{C}H_2$- and $\mathbf{C}_\alpha$-CH_2 of styrene, respectively, in pure SBR. Indeed, different types of unsaturation in

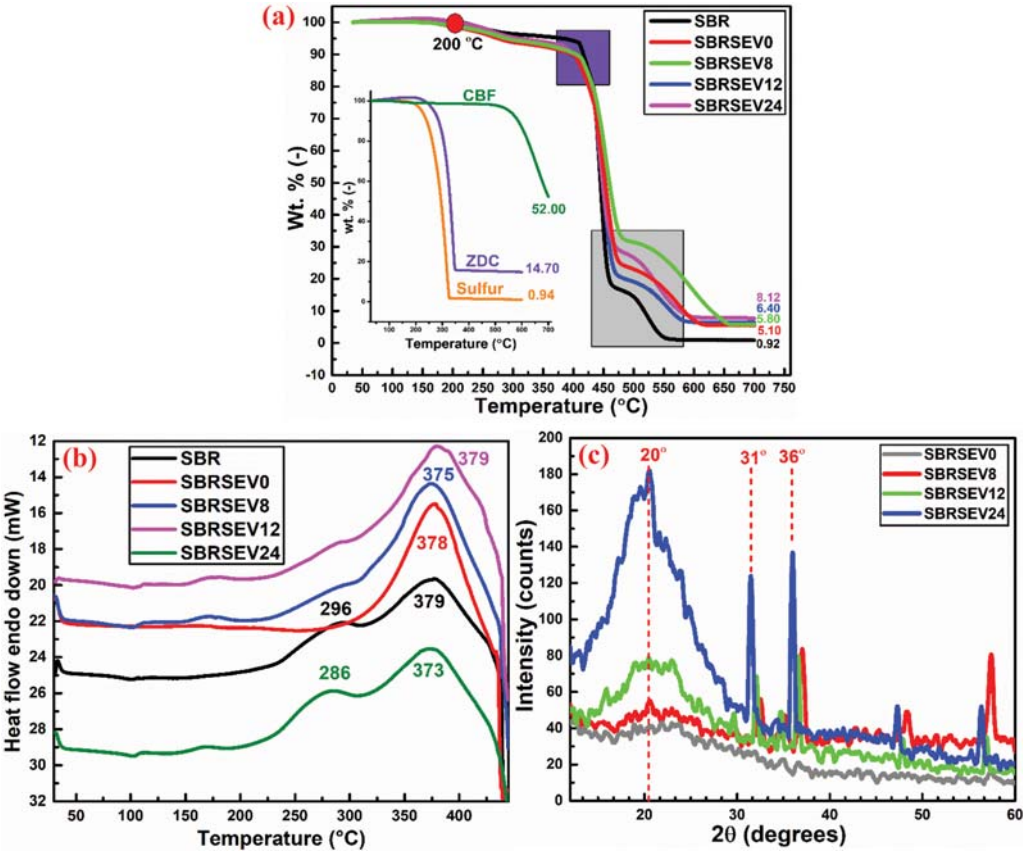

Fig. 2. (a) TGA of SBR/SBRSEV0/8/12/24, (inset of a) TGA of S/ZDC/CBF; (b) DSC of SBR/SBRSEV0/8/12/24 and (c) XRD of SBR/SBRSEV0/8/12/24.

SBR, resulting from the reaction between styrene and 1,3 butadiene, were emphasized from characteristic peaks at 132.90, 129.82, 127.52 and 116.07 ppm for CH_2=**C**H- of vinyl, -**C**H=**C**H- (*trans*), -**C**H=**C**H- (*cis*) and **C**H_2=CH- of vinyl, respectively. In addition, the symbolic peaks of >**C**H- adjacent to CH_2=CH-, -**C**H_2- adjacent to -CH=CH- (*trans*) and -CH=CH- (*cis*) were noted at 37.36, 34.37, 31.89/29.16, respectively. The characteristic peaks at 149.39, 131.53 and 129.31 ppm for aromatic carbons of styrene indicated the non-involvement of aromatic carbons in vulcanization. Most importantly, the disappearance of olefinic backbone specific peaks at 132.90, 129.82, 127.52 and 116.07 ppm in SBRSEV0, along with the arrival of symbolic intense peak at 51.03 ppm for C-S crosslinking [33], implied the vulcanization through sulfur in SBRSEV0 network, also ascertained from FTIR, TGA, DSC, XRD, SEM and DFT analyses. Such crosslinking was also corroborated from the drastic drop in intensity of -**C**H_2- specific peak at 34.37 of SBR to 34.46 ppm in SBRSEV0 by the vulcanization process. Moreover, peaks at 45.14, 41.21 and 40.10 ppm appeared in SBRSEV0 due to >**C**H-, -**C**H_2- and **C**$_\alpha$-CH_2 of styrene, respectively. In addition, symbolic peaks of -**C**H_2- adjacent to -CH=CH- (*trans*), -CH=CH- (*cis*) and >**C**H- were noted at 34.46, 32.15/29.24 and 38.22 ppm, respectively, as compared to 34.37, 31.89/29.16 and 37.36 ppm of SBR in consequence to indirect deshielding effect imposed by C-S crosslinks.

3. Thermal Analysis by TGA

From TGA diagram (Fig. 2(a)), three major weight loss regions [34], within 1.00-4.52, 4.52-82.35 and 82.35-99.38 wt% for SBR and 1.00-7.23, 7.23-79.33 and 79.33-94.9 wt% for both unfilled and filled SBRSEVs were observed with onset at around 200 °C [6]. In fact, the weight loss from 200 to 350 °C for all the membranes was ascribed to the removal of volatile components, such as stearic acid and physically adsorbed moisture [35]. The initial major weight loss was related to the degradation of SBR backbone into gaseous products. In the second stage, weight loss was associated with scission of crosslinked and filed SBRSEVs. In fact, such degradation continued up to 660 °C for SBRSEVs [28]. In this context, the amount of residues for S, ZDC and CBF was found to be 0.94, 14.70 and 52.00 wt%, respectively (inset of Fig. 2(a)). Therefore, the percentage residue of 0.92 wt% for SBR was found to be exceptionally low in comparison to 5.10-8.12 wt% of filled and crosslinked membranes, signifying the presence of inorganic residues of ZDC and CBF. Indeed, the amounts of residues were found to be 5.10, 5.80, 6.40 and 8.12 wt% for SBRSEV0, SBRSEV8, SBRSEV12 and SBRSEV24, respectively, related to the enhancement of CBF in membranes. The maximum decomposition rate of SBRSEV0 signified the least thermal stability as compared to that of other composite membranes at comparable decomposition temperatures. Altogether, the thermal stability was found to increase remarkably with vulcanization and crosslinking/CBF loading.

4. Thermal Analysis by DSC

The DSC curves for SBR, SBRSEV0 and composite SBRSEVs in N_2 atmosphere showed exothermic peaks within 350-400 °C, along with the appearance of a shoulder peak within 286-296 °C. From Fig. 2(b), the appearance of intense and broad exothermic peaks within 373-379 °C for both SBR and SBRSEVs was ascribed to the volatilization of non-CBF organic and CBF additives from the tighter rubber network [36]. As compared to SBR, more intense endothermic peaks of SBRSEV0 and composite SBRSEVs could be ascribed to the increased compactness between rubber chains, rendering the immobilization of chains via formation of C-S bonds in rubber matrix. Moreover, the introduction of crosslinking resulted in the complete disappearance of shoulder peaks at 296 °C as compared to SBR that reappeared in composite SBRSEVs. Eventually, the peak area was found to increase with gradual incorporation of CBF into the SBRSEVs. The appearance of exothermic peak could be attributed to the volatilization of some components, such as moisture, plasticizer, residual solvents, oils and low boiling components/volatile matters.

5. Variation of Mechanical Strength and Crosslink Densities

Uncrosslinked SBR membranes are soluble in hydrocarbon solvents, such as toluene and THF. However, for higher extent of crosslinking, only restricted swelling occurs. For a given degree of crosslink density, a better solvent will give higher swelling. Such measurements are possible from quantitative expression of Flory-Rehner Eq. (21) [9].

$$v = \frac{1}{V_s}\left[\frac{\ln(1-v_r)+v_r+\chi_{1p}v_r^2}{\frac{1}{2}v_r-v_r^{1/3}}\right] \tag{21}$$

Here v, V_s, v_r and χ represent crosslink density, molecular volume, volume fraction and interaction parameters, respectively. Crosslink density is determined by the following equation of kinetic theory of elasticity [9].

$$\sigma = RTv\left(\lambda' - \frac{1}{\lambda'^2}\right) \tag{22}$$

Here, σ and v represent the stress to extend the crosslink rubber sample to extension ratio λ' and number of crosslinks in 1 cm^3, respectively. The variation of crosslink densities, TS, EAB and modulus of filled-/unfilled-SBRRSEV membranes are given in Table 4. An enhancement of physical crosslink densities from SBRSEV0 to SBRSEV24 was attributed to the presence of weak secondary force of attraction between functional groups of CBF and rubber chains via surface active filler loading (Scheme S1). Unlike physical crosslink densities, noticeable change in chemical crosslink densities (Table 4) could not be observed. This might so happen by the use of identical A/S ratio during crosslinking. Again, mechanical properties of the used membranes were expected to increase by the use of increasing amount of surface reinforcing CBF. This eventually justified the enhancement of TS and modulus from SBRSEV0 to SBRSEV24 with the simultaneous decrease in EAB. Thus, RSM was utilized to optimize TS and EAB.

6. XRD Analysis

The introduction of regular three-dimensional repeated positioning of similar miller planes, a set of parallel planes, in a space lattice enhances mechanical properties of solids [40]. The mechanical properties of used membranes followed the order: SBRSEV24> SBRSEV12>SBRSEV8>SBRSEV0>SBR, which was confirmed by the successive increase in peak intensities of pure, vulcanized and composite membranes (Fig. 2(c)) [8]. In this context, pure SBR showed a characteristic broad diffraction peak at 2θ=20°, which

Table 4. Physical properties of membranes

Membrane/ thickness (μm)	CD*×10^4 (mol cm^{-3}) (chemical method)	CD* (MPa) (physical method)	Modulus (MPa)/ %elongation	TS (MPa)/ EAB (%)	Ref.
EPDMCV[a]/50	9.50	0.49	0.34/100	4.46/750.0	[9]
EPDMSEV[a]/50	11.20	4.12	0.41/100	5.31/670.0	[9]
EPDMEV[a]/50	14.10	5.43	0.53/100	7.87/530.0	[9]
EPDM0[a]/50	4.89	6.45	0.34/100	4.46/750.0	[8]
EPDM2[a]/50	7.20	10.65	0.48/100	6.24/337.3	[8]
EPDM4[a]/50	8.83	13.56	0.57/100	7.15/245.2	[8]
EPDM6[a]/50	9.30	14.56	0.62/100	7.89/172.1	[8]
PDMS[b]/33	-	-	-/-	1.82/94.80	[37]
PDMS[b]/85	-	-	-/-	1.91/120.2	[37]
PDMS[b]/189	-	-	-/-	1.97/198.9	[37]
PDMS[b]/285	-	-	-/-	2.12/250.7	[37]
EPDM[a]/-	-	-	1.40/200	2.40/388.5	[38]
NR1[c]/30	1.10	1.73	0.53/100	7.87/530.0	[39]
NR2[c]/30	0.90	1.36	0.41/100	5.31/670.0	[39]
NR3[c]/30	0.70	1.04	0.34/100	4.46/750.0	[39]
SBR1/30	1.40	1.89	0.63/100	2.77/370.0	[39]
SBR2/30	1.00	1.21	0.48/100	1.93/490.0	[39]
SBR3/30	0.90	0.97	0.42/100	1.43/540.0	[39]
SBRSEV0/50±0.55	2.99	2.63	0.56/100	5.80/500.0	TW[#]
SBRSEV8/50±0.55	3.25	3.52	1.14/100	6.25/486.0	TW
SBRSEV12/50±0.55	3.59	4.34	1.64/100	6.87/454.0	TW
SBRSEV24/50±0.55	3.97	5.37	1.76/100	7.13/440.0	TW

[a]Ethylene propylene diene monomer
[b]Polydimethylsiloxane
[c]Natural rubber
*Crosslink density and #this work

was related to its inferior mechanical properties. In fact, the enhancement of physicochemical properties with CBF loading was also reflected from the respective TGA diagram (Fig. 2(a)). However, CBF of high surface area resulted in enhanced physical-/chemical-crosslink density, TS and modulus and hence, mechanical property, as a result of filling of voids in vulcanized membranes. Meanwhile, the radial distances evaluated by RDF analyses for a single layer of graphene were almost identical to the Miller distances (d_{100}= 2.45 Å, for n=1, 1st order/d_{200}=3.80 Å, for n=2, 2nd order etc.), determined from sharp symbolic XRD peak intensities in the proximity of 2θ=31°/36° in all composite membranes. In fact, SBRSEV0 exhibited the lowest dimensional stability due to the absence of any physical crosslinking, as evident from minimum peak intensity in XRD.

7. FESEM and EDX Analyses

The change in surface morphology of used membranes due to the distribution of CBF within rubber matrix was determined from FESEM photomicrographs at higher magnifications (10 kX). The featureless dense surface morphology of SBRSEV0 was ascribed to the closeness of rubber chains via bi-/poly-sulfidic linkages (Fig. 3(a)), introduced through crosslinking in accelerated vulcanization. At lower wt% of CBF loading, particles were equally distributed and, thus, resulted in uniform morphology [8]. However, morphology coarsening via uneven distribution of CBFs through particle agglomeration was observed by the gradual enhancement of CBFs from SBRSEV8 to SBRSEV24 due to relative lowering in the extent of compatibility with rubber matrix. In fact, such coarsening became more intense with the successive increase in the amounts of CBF in membranes (Fig. 3(b)-(d)). Indeed, the rough surface and uneven distribution of CBFs in composite membranes introduced more voids by the strong filler-filler interaction [41]. However, the relative peak intensities of Zn:S in EDX (inset of Fig. 3(a)) supported the ZDC:S ratio used for vulcanization via SEV.

8. Variations of State-I/II/III Activity Coefficients of THF and Water, Interaction Parameters, Total Sorption (TS) and Sorption Selectivity (SS) with Feed Concentration of THF

The variation of activity coefficients of THF and water with feed concentration is given in Fig. 4(a) and 4(b), respectively. The preferential separation of one component from a binary mixture could rationally be understood by comparing liquid-liquid and liquid-membrane interactions. However, the best way to elucidate the coupling effect is to study the change in activity coefficient of each component in the thermodynamic swelling process. In this regard, such change in activity coefficient might be brought about by two types of coupling: interaction of each component with membrane and mutual interaction between components in membrane. Separation of solvent mixture by preferential sorption occurs only when interaction of a particular solvent with membrane matrix dominates

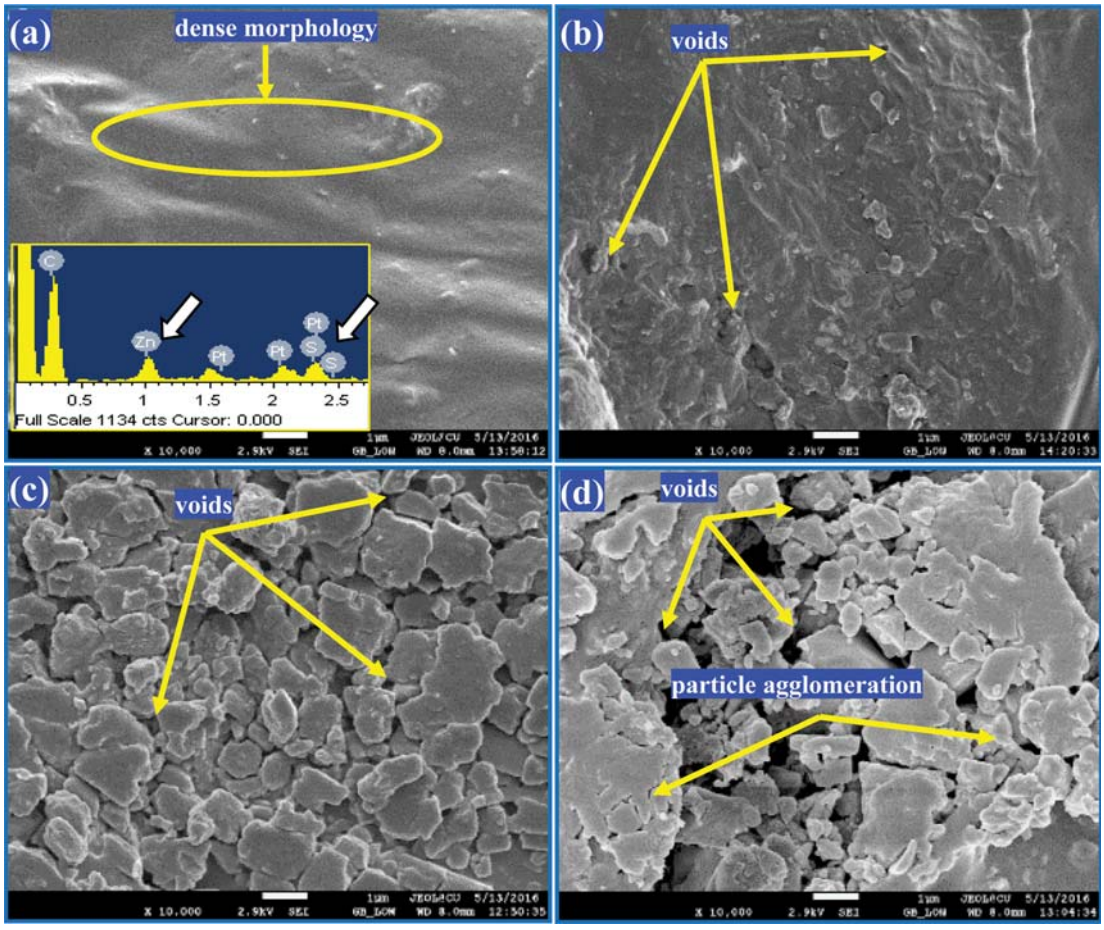

Fig. 3. FESEM photomicrographs of (a) SBRSEV0, (b) SBRSEV8, (c) SBRSEV12 and (d) SBRSEV24 and (inset of a) EDX of SBRSEV0 membrane.

over mutual interaction between solvents. To estimate the contribution of coupling effect, three different curves of activity coefficients were considered: state-I, describing the activity coefficient of pure component within the membrane, is considered as reference, state-II relates activity coefficients with respect to the reference state to account for the possible interaction of each component with membrane matrix only, and state-III illustrates the mutual interaction of both the components within membrane. The deviation of state-I from state-II demonstrates the interaction between each component and membrane matrix with the change in feed concentration, whereas difference between state-II and state-III determines the contribution of coupling effect between two components within the membrane [9].

From Fig. 4(a), the deviation of state-I from state-II was higher than that of state-II and state-III, indicating better interaction between THF and membrane than the prevalent mutual interaction with water, justifying the selective removal of THF from THF-water mixtures [42]. However, poor water selectivity of membranes was rationalized from larger deviation between state-II and state-III than state-I and state-II (Fig. 4(b)). From Fig. 4(a), it was also observed that such deviation decreased with increasing feed concentration and, thus, resulted in poor THF selectivity. However, the deviation between state-II and state-III for THF was increased with the increase in amount of CBF, which indicated the enhancement of organoselectivity. The variation of interaction parameters between THF and water in feed (χ_{12}^{f}) and membrane (χ_{12}^{m}) with feed THF is shown in Fig. 4(c). In addition, interaction parameters of solvents in membrane phase were determined by plotting χ_{12}^{f} versus volume fraction of THF (V_1) in feed to obtain a polynomial trend line $30.25u_1^2-7.841u_1+7.0026$. As mutual solvent-solvent interaction is inversely proportional to interaction parameters, lower value of interaction parameter specifies the higher mutual interaction between solvents. Since, χ_{12}^{m} for all the membranes were higher than χ_{12}^{f}, the decrease in mutual interaction between the components in the membrane phase resulted in the thermodynamically favorable separation. Fig. 4(c) also showed that χ_{12}^{m} increased with the increasing amount of organophilic CBF, indicating lower extent of mutual interaction between 1 and 2 in membrane phase as compared to the feed. Thus, separation of THF became more spontaneous through the rubber membranes containing higher amount of CBF. In addition, with the increase in feed concentration of THF, χ_{12}^{m} of THF and water were observed to increase, whereas a reverse trend was observed for χ_{12}^{f}. Thus, THF recovery was expected to be easier with increasing feed. However, higher amount of THF caused plasticization of the organophilic rubber membranes that allowed more water to pass through the membrane and thus, caused a decrease in

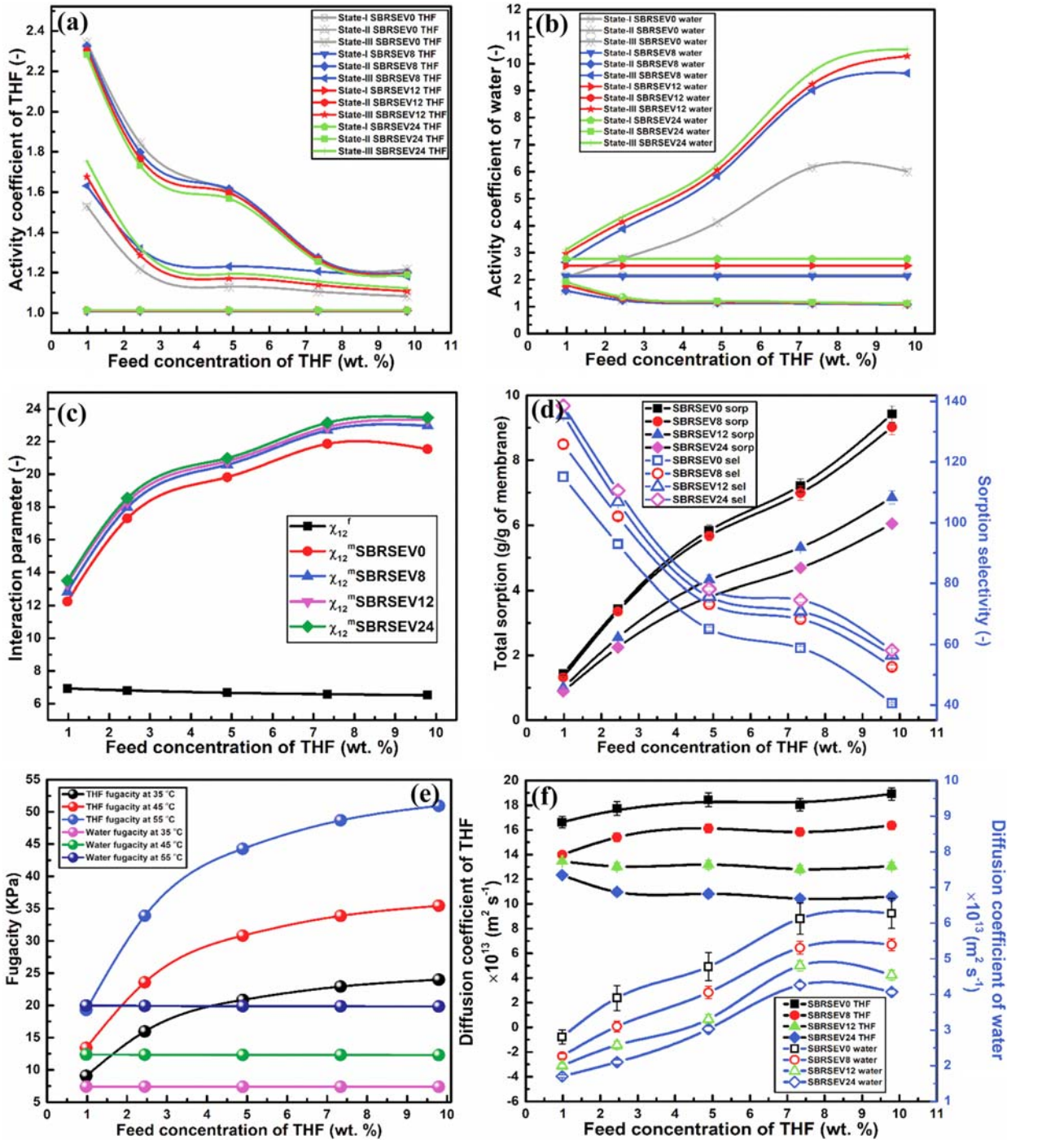

Fig. 4. Variation of state-I/II/III activity coefficients of (a) THF and (b) water (c) interaction parameters and (d) total sorption/sorption selectivity with feed concentration of THF and effect of feed concentration of THF on (e) fugacity and (f) diffusion coefficient.

SF. The covalent interaction between pyrones, chromenes and ketones of CBF and THF resulted in an alleviated sorption of THF by the rubber membranes containing higher amount of organophilic CBF. This could presumably be attributed to better compatibility in the positioning of aromatic phenyl ring and heterocyclic THF. The external graphitic surface is generally composed of basal-plane carbon atoms held together in the form of hexagons. In this context, the flat configuration of benzene rings, in which six carbon atoms are in a hexagonal plane, would fit better on the graphitic surface of CBF.

The variation of total sorption and sorption selectivity of THF for the used membranes as a function of feed concentration at 35 °C are shown in Fig. 4(d), in which total sorption and sorption selectivity were found to follow an opposite trend with increasing feed concentration. Such reverse variation of total sorption and sorption selectivity with feed was reported earlier by Singha et al. [8].

However, organophilic SBRSEV membrane networks, both filled and unfilled, were sustained within 0.97-9.79 wt% of THF in water. From Fig. 4(d), total sorption was observed to increase rapidly with increasing feed concentration due to higher degree of swelling by preferential interaction between THF and organophilic rubber membranes, attributed to the closeness of solubility parameters of THF (19.2 $MPa^{0.5}$) and SBRSEVs (17.00-16.99 $MPa^{0.5}$). Again, introduction of CBF in rubber membranes introduced significant changes in the composite membrane networks. In fact, organophilic CBF played the role of physical crosslinker and restricted the sorption of polar water molecules. Therefore, filled and crosslinked rubber membranes are more suitable for THF sorption than mere crosslinked membranes. In this regard, total sorption and sorption selectivity of SBRSEV24 membrane were found to be 0.8851±0.0028 (g g^{-1} of membrane) and 138.6±1.3, respectively, at 0.97 wt% of THF in feed.

9. Design of Experiments

RSM is widely used for modelling and optimization of responses, executed principally by performing the minimum number of predesigned experiments [43], followed by estimating the coefficients through a mathematical model, and finally, predicting the responses and examining the adequacy of the chosen model [44]. Face-centered central composite design (FCCCD), a standard RSM design, was applied to optimize the individual and interactive effects of independent variables on the responses. The following second-order empirical polynomial equation (Eq. (23)) is usually applied to analyze and correlate response with input variables for optimization.

$$Y = \beta_0 + \sum_{i=1}^{3}\beta_i X_i + \sum_{i=1}^{3}\beta_{ii} X_i^2 + \sum_{i=1}^{3}\sum_{j=1}^{2}\beta_{ij} X_i X_j \quad (23)$$

Here, Y, β_0, β_i, β_{ii} and β_{ij} represent predicted response, constant, linear, quadratic and interaction coefficients, respectively. To justify the significance/adequacy of the predicted model by analysis of variance (ANOVA), independent experimental conditions were taken as coded variables from −1 to +1 to develop the regression model. In this study, optimization of TS/EAB, TF/SF and partial permeabilities of 1/2 was performed independently, using FCCCD by taking wt% of accelerator (A)/sulfur (B) and temperature of experiment (X_1)/wt% of feed THF (X_2)/filer (X_3) as input variables (Table 5). Data obtained from experiments were fitted to the above equation for determining regression coefficients (R^2).

Table 5. Maximum and minimum data ranges of input parameters used in three step RSM

Parameters	Maximum range (−1)	Minimum range (+1)
X_1	35 °C	55 °C
X_2	0.97	9.79
X_3	0	24
A	2 wt%	6 wt%
B	2 wt%	6 wt%

10. RSM Optimization of Individual and Interactive Effects of Variables on TS and EAB

The experimental design for determining the optimum A/S ratio required in vulcanization is given in Table 6. The FCCCD based optimization on A and B produced Eqs. (24) and (25).

$$R_{TS} = 5.41 + 0.46A - 0.18B - 0.01AB - 0.02A^2 + 0.01B^2 \quad (24)$$

$$R_{EAB} = 534.68 - 109.46A + 74.79B - 0.50AB + 9.47A^2 - 6.90B^2 \quad (25)$$

The ANOVA for optimization of TS and EAB, obtained by employing Eq. (24) and (25) is given in Table 7. The response surface and optimization plots of TS and EAB are given in Fig. 5(a)-(c). The variation of TS and EAB with wt% of S and A is displayed in Fig. 5(a) and 5(b), respectively. However, TS/modulus and EAB showed an opposite trend with increasing wt% of S and A that was corroborated with the arrival of better mechanical properties, via incorporation of surface reinforcing CBF in rubber matrix, and thereby restricted the flexibility of rubber moieties [9]. Eventually, the perfect balance between TS and EAB was essential to develop the mechanically strong and dimensionally stable SBR membranes [5]. Thus, RSM was employed to evaluate the optimum A/S ratio, obtained by considering A, B, TS and EAB 'in range' in the numer-

Table 6. Design matrix and responses for TS and EAB

Runs	Uncoded (Coded) values		TS (MPa)		EAB (%)	
	A (wt%)	S (wt%)	Actual	Predicted	Actual	Predicted
1	2 (−1)	2 (−1)	5.88	5.88	460	473.63
2	6 (+1)	2 (−1)	6.88	6.88	340	334.97
3	2 (−1)	6 (+1)	5.58	5.43	520	547.97
4	6 (+1)	6 (+1)	6.40	6.25	392	401.29
5	2 (−1)	4 (0)	5.46	5.61	580	538.40
6	6 (+1)	4 (0)	6.36	6.51	400	395.74
7	4 (0)	2 (−1)	6.47	6.47	375	366.40
8	4 (0)	6 (+1)	5.63	5.93	474	436.74
9	4 (0)	4 (0)	6.22	6.16	420	429.17
10	4 (0)	4 (0)	6.22	6.16	420	429.17
11	4 (0)	4 (0)	6.22	6.16	420	429.17
12	4 (0)	4 (0)	6.22	6.16	420	429.17
13	4 (0)	4 (0)	6.22	6.16	420	429.17

Table 7. ANOVA for TS/EAB

Source	Sum of squares	df[#]	Mean square	*F* value	*P*-value
Model	1.700/42493.43	5/5	0.340/8498.69	11.69/12.63	0.0027[*]/0.0022[*]
A	1.230/30530.67	1/1	1.230/30530.67	42.29/45.36	0.0003[*]/0.0003[*]
B	0.440/7420.17	1/1	0.440/7420.17	15.00/11.02	0.0061[*]/0.0128[*]
AB	0.008/16.00	1/1	0.008/16.00	0.28/0.02	0.6144/0.8818
A^2	0.025/3966.51	1/1	0.025/3966.51	0.86/5.89	0.3851/0.0456[*]
B^2	0.006/2104.43	1/1	0.006/2104.43	0.19/3.13	<0.6758/0.1203
Residual	0.2/4711.49	7/7	0.029/673.07		
Lack of fit	0.2/4711.49	3/3	0.068/1570.5		
Pure error	0.00/0.00	4/4	0.00/0.00		
Cor total	1.91/47204.92	12/12			

[*]Significant and [#]degrees of freedom

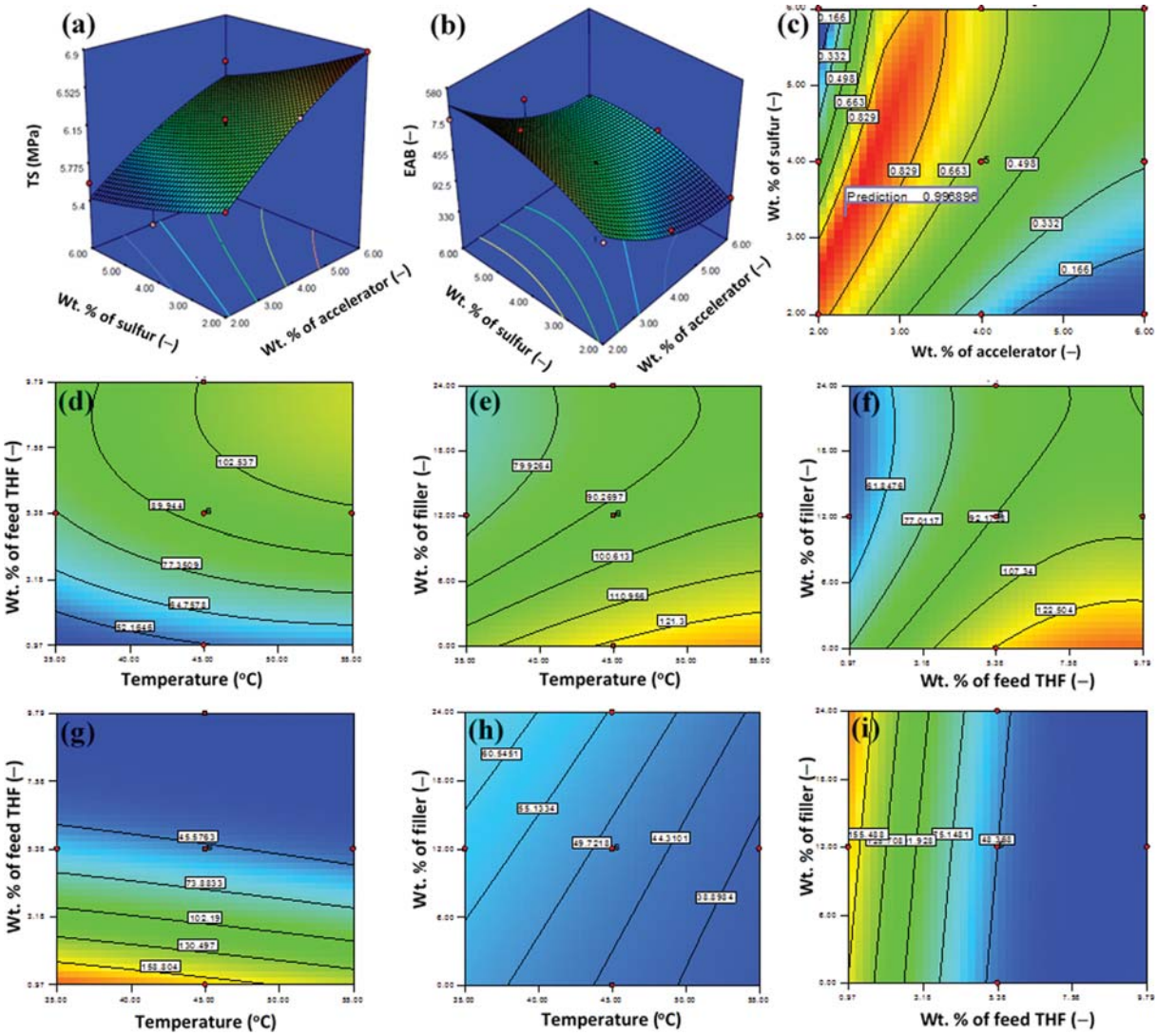

Fig. 5. The 3D response surface plots of (a) TS/(b) EAB and (c) desirability plot and the 2D contour plots of R_{TF}/R_{SF} versus (d/g) wt% of feed THF/temperature, (e/h) wt% of filler/temperature and (f/i) wt% of filler/wt% of feed THF.

ical optimization section. From Fig. 5(c), the optimum values of input variables were 2.32/3.29 wt% of A/S (A/S=0.71), which belonged to the range of SEV. Thus, semi-efficiently crosslinked and filled membranes were used for THF separation.

Table 8. Design matrix and response data for partial permeabilities of THF-water and SF/TF optimization using FCCCD model of RSM

	Run	X_1 Uncoded (coded)	X_2 Uncoded (coded)	X_3 Uncoded (coded)	PP_{THF} ($\times 10^8$ Barrer)		PP_{water} ($\times 10^8$ Barrer)		TF ($g\ m^{-2}\ h^{-1}$)		SF (-)	
					Actual	Predicted	Actual	Predicted	Actual	Predicted	Actual	Predicted
Full factorial portion	1	35.00 (−1)	0.97 (−1)	0.00 (−1)	6.14	6.12	4.39	4.28	63.56	65.24	170.36	172.99
	2	55.00 (+1)	0.97 (−1)	0.00 (−1)	3.53	3.39	2.50	2.47	84.98	82.32	135.35	136.16
	3	35.00 (−1)	9.79 (+1)	0.00 (−1)	5.35	5.21	5.16	5.16	119.66	117.51	30.55	27.63
	4	55.00 (+1)	9.79 (+1)	0.00 (−1)	2.86	2.87	3.15	3.09	149.88	150.21	21.08	26.76
	5	35.00 (−1)	0.97 (−1)	24.00 (+1)	3.80	3.79	2.22	2.30	36.71	36.90	208.33	202.46
	6	55.00 (+1)	0.97 (−1)	24.00 (+1)	2.18	2.33	1.32	1.34	49.17	51.84	158.94	161.67
	7	35.00 (−1)	9.79 (+1)	24.00 (+1)	2.99	3.13	3.34	3.39	69.27	72.45	26.39	25.40
	8	55.00 (+1)	9.79 (+1)	24.00 (+1)	2.05	2.07	2.04	2.17	104.18	103.02	23.39	20.58
Axial portion	9	35.00 (−1)	5.38 (0)	12.00 (0)	3.99	4.02	3.45	3.44	79.81	76.90	51.39	58.53
	10	55.00 (+1)	5.38 (0)	12.00 (0)	2.17	2.12	1.99	1.93	99.92	100.73	44.12	37.70
	11	45.00 (0)	0.97 (-1)	12.00 (0)	3.47	3.49	2.22	2.26	53.27	51.38	168.21	167.91
	12	45.00 (0)	9.79 (+1)	12.00 (0)	2.93	2.90	3.23	3.11	103.32	103.11	23.65	24.68
	13	45.00 (0)	5.38 (0)	0.00 (−1)	3.88	4.16	3.65	3.85	120.21	123.00	49.32	43.11
	14	45.00 (0)	5.38 (0)	24.00 (+1)	2.89	2.59	2.67	2.40	90.13	85.24	47.82	54.75
Center portion	15	45.00 (0)	5.38 (0)	12.00 (0)	3.01	3.01	2.71	2.73	91.92	92.62	48.56	48.32
	16	45.00 (0)	5.38 (0)	12.00 (0)	3.01	3.01	2.71	2.73	91.92	92.62	48.56	48.32
	17	45.00 (0)	5.38 (0)	12.00 (0)	3.01	3.01	2.71	2.73	91.92	92.62	48.56	48.32
	18	45.00 (0)	5.38 (0)	12.00 (0)	3.01	3.01	2.71	2.73	91.92	92.62	48.56	48.32
	19	45.00 (0)	5.38 (0)	12.00 (0)	3.01	3.01	2.71	2.73	91.92	92.62	48.56	48.32
	20	45.00 (0)	5.38 (0)	12.00 (0)	3.01	3.01	2.71	2.73	91.92	92.62	48.56	48.32

11. Verification of Individual and Interactive Effects of Input Variables on TF and SF

The experimental design for estimating the optimum TF and SF for THF-water separation is given in Table 8. The numerical optimization was carried out by taking X_1, X_2, X_3 and TF 'in range' and SF 'maximize'. The acceptability of this model was expressed by the attainment of high and low values of F and p, respectively (Table 9). In fact, p values of X_1, X_2 and X_3 were less than 0.05 and, thus, considered to be significant at 95% confidence level. Indeed, the statistical analyses evolved the following two empirical expressions for TF and SF.

$$R_{TF}=-48.15+4.19X_1+11.33X_2-2.87X_3+0.09X_1X_2 -0.004X_1X_3-0.08X_2X_3-0.04X_1^2-0.79X_2^2+X_3^2 \quad (26)$$

$$R_{SF}=279.93-1.86X_1-50.16X_2+1.56X_3+0.20X_1X_2 +0.008X_1X_3-0.15X_2X_3+0.002X_1^2+2.47X_2^2+0.004X_3^2 \quad (27)$$

The ANOVA (Table 9) for SF showed high F=260.37, confirming good applicability of model. In fact, linear (X_1, X_2, X_3), interactive (X_1X_2, X_2X_3), and quadratic (X_3^2) terms were significant for SF (Table 9). Again, high R^2 of both responses, 0.9938 and 0.9958 for R_{TF} and R_{SF}, respectively, indicated better correlation between experimental and predicted responses. The closeness of adj. R^2, 0.9882 and 0.9919 for R_{TF} and R_{SF}, respectively, and pred. R^2 of 0.9264 and 0.9542 for R_{TF} and R_{SF}, respectively, indicated fair aptness of this model [45]. Adequate precision values of responses, 56.41 and 48.66 for R_{TF} and R_{TF}, respectively, signified good applicability of this model to navigate the design space. In addition, relatively lower coefficients of variation, 3.20% and 7.29% for R_{TF} and R_{SF}, respectively, suggested the preciseness and reliability of the experiment [45]. The interactive effects of these variables on R_{TF} and R_{SF} are shown in Fig. 6(a)-(f). Indeed, such effects of independent variables were also reflected in 3D response surface and 2D contour plots (Fig. 5(d)-(i)).

Fig. 6(a)-(c) indicated the combined effect of X_1/X_2, X_1/X_3 and X_2/X_3 on TF. The combined influence of X_1 and X_2 (Fig. 6(a)) increased TF steadily by the increase in X_1 from 35 to 45 °C. However, such effect became more prominent at much higher feed concentration. The significant increase in TF for the filled SBRSEV membranes was attributed to plasticization and, hence, increase in segmental motion of organophilic membranes at high feed concentration, imparting lesser restriction for permeation of both components. The effect of chain loosening via plasticization was more pronounced at higher temperature, resulting in the maximum TF at 9.79 wt% of THF and 55 °C. In contrast, SF decreased slightly with rise in temperature and predominantly with feed concentration, resulting in the maximum at 0.97 wt% of THF and 35 °C. In addition, SF decreased linearly with increase in temperature due to much higher permeation rate resulting from lower kinetic diameter of water than THF [2]. Again, TF decreased with the increase in CBF (Fig. 6(b)), whereas for a fixed amount of CBF, rise in temperature elevated TF. However, TF and SF became the maximum at 55 °C/0 wt% of CBF and 35 °C/24 wt% of CBF, respectively. In addition, the rise in temperature from 35 to 55 °C and decrease in CBF from 24 to 0 wt% showed a comprehensive decrease in SF. However, TF was found to increase predominantly at relatively

Table 9. ANOVA of the second order polynomial models according to RSM-FCCCD studies on partial permeabilities of THF-water and TF/SF

Source	Sum of squares	df#	Mean square	*F* value	*P*-value
			PP_{THF}/PP_{water}/TF/SF		
Model	18.35/13.79/ $1.28\times10^4/6.55\times10^4$	9	2.04/1.53/ $1431.15/7.27\times10^3$	79.95/85.81/ 177.35/260.37	$<0.0001^*/<0.0001^*/$ $<0.0001^*/<0.0001^*$
X_1	8.99/ 5.72/ $1.42\times10^3/1084.51$	1	8.99/5.72/ $1418.96/1.08\times10^3$	352.49/320.10/ 175.84/38.80	$<0.0001^*/0.0001^*/$ $<0.0001^*/<0.0001^*$
X_2	0.86/1.82/ $6.68\times10^3/5.13\times10^4$	1	0.86/1.82/ $6688.43/5.13\times10^4$	33.90/102.12/ $828.84/1.83\times10^3$	$0.0002^*/0.0001^*/$ $<0.0001^*/<0.0001^*$
X_3	6.16/5.27/ $3.56\times10^3/338.84$	1	6.16/5.72/ 3565.68/338.84	241.69/295.20/ 441.87/12.12	$0.0001^*/<0.0001^*/$ $<0.0001^*/<0.0059^*$
X_1X_2	0.08/0.03/ 122.07/646.74	1	0.08/0.03/ 122.07/646.74	3.14/1.89/ 15.13/23.14	$0.1069/0.1989/$ $0.0030^*/0.0007^*$
X_1X_3	0.81/0.36/ 2.28/7.82	1	0.81/0.36/ 2.28/7.82	31.63/20.23/ 0.28/0.28	$0.0002^*/0.0011^*/$ 0.6067/0.6084
X_2X_3	0.03/0.022/ 139.70/502.60	1	0.03/0.02/ 139.70/502.60	1.33/1.23/ 17.31/17.98	0.2764/0.2925/ $0.0019/0.0017^*$
X_1^2	$9.30\times10^{-3}/7.38\times10^{-3}/$ 39.82/0.11	1	$9.90\times10^{-3}/7.38\times10^{-3}/$ 39.82/0.11	0.37/0.41/ $4.94/3.94\times10^3$	0.5591/0.5346/ 0.0506/0.9512
X_2^2	$0.087/6.02\times10^{-3}/$ $650.11/6.33\times10^3$	1	$0.09/6.0310^{-3}/$ $650.11/6.33\times10^3$	3.42/0.34/ 80.56/226.46	0.0940/0.5741/ $<0.0001^*/<0.0001^*$
X_3^2	0.36/0.41/ 363.66/1.04	1	0.36/0.41/ 363.66/1.04	14.23/23.21/ 45.07/0.04	$0.0039/0.0007^*/$ <0.0001/0.8509
Residual	0.25/0.18/ 80.70/279.49	10	0.02/0.02/ 8.07/27.95		
Lack of fit	0.25/0.18/ 80.70/279.49	5	0.05/0.03/ 16.14/55.90		
Pure error	0.00/0.00/ 0.00/0.00	5	0.00/0.00/ 0.00/0.00		
Cor total	18.60/13.97/ $1.30\times10^4/6.58\times10^4$	19			
Std. dev.	0.16/0.13/ 2.84/5.29		R^2	0.9863/0.9872/ 0.9938/0.9958	
Mean	3.31/2.88/ 88.78/72.51		Adj. R^2	0.9740/0.9757/ 0.9882/0.9919	
CV %	4.82/4.64/ 3.20/7.29		Pred. R^2	0.8608/0.8931/ 0.9264/0.9542	
Press	2.59/1.49/ 953.83/3.01×10^3		Adeq. precision	35.906/40.408/ 56.412/48.655	

*Significant and #degrees of freedom (same for all responses)

lower wt% of CBF (Fig. 6(b)). In fact, TF increased with feed concentration and became the maximum at 9.79 wt% of THF for SBRSEV0. However, SBRSEV24 showed the maximum SF at low concentration of THF, decreasing significantly with increase in feed concentration (Fig. 6(c)). The incorporation of CBF decreased the available voids within rubber matrix by physical crosslinking, as also evident from FESEM (Fig. 3(b)-(d)), allowing both the components to pass through a tortuous path. Thus, TF decreased with the increase in SF due to such restrictive permeation of both components. These vulcanized and filled SBR membranes showed the minimum TF of 36.900 g m^{-2} h^{-1} and the maximum SF of 202.461 at 35 °C, 0.97 wt% of THF and 24 wt% of CBF with excellent desirability of 0.969. To test the reproducibility of the obtained results, SD of the replicate analysis was also evaluated. However, the regressed equations were validated by taking input variables of the pervaporation experiment, avoiding the data used in RSM. The predicted TF and SF were plotted with the experimental data (Fig. 6(g)-(j)). The adj. R^2 and *F* values were found to be as high as 0.9922/0.9902 and 1896.69/1519.03 for TF/SF that indicated the rational applicability of the RSM generated quadratic models.

12. Verification of Individual and Coupled Effects of Input Parameters on Partial Permeabilities of THF and Water

The 3D response surface plots and validation diagrams for both partial permeabilities are given in Fig. 7(a)-(f) and (j)-(k), respec-

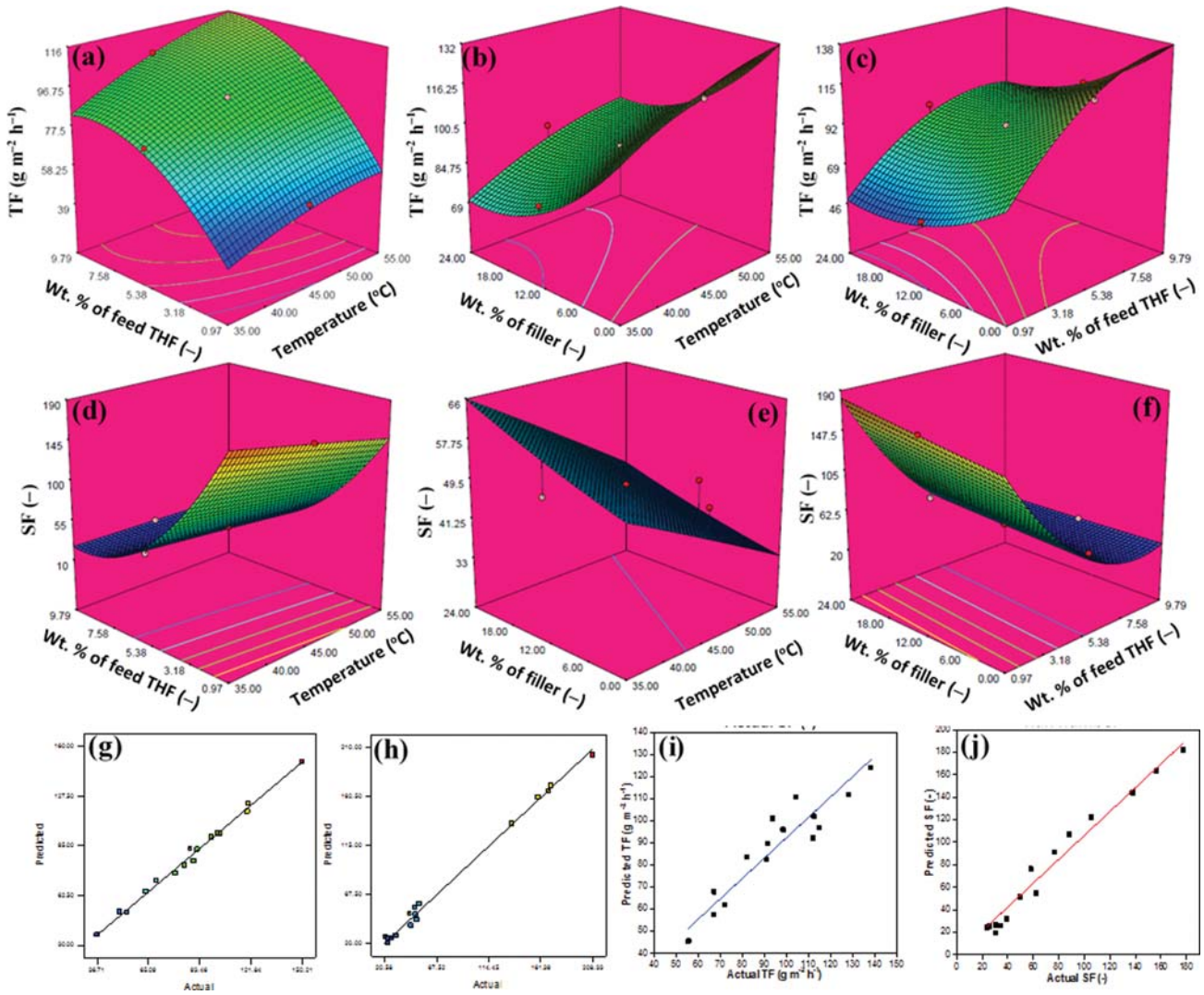

Fig. 6. The 3D response surface plots of R_{TF}/R_{SF} versus (a/d) wt% of feed THF/temperature, (b/e) wt% of filler/temperature, (c/f) wt% of filler/wt% of feed THF, (g/h) actual versus predicted plots of TF/SF and (i/j) validation plots of TF/SF.

tively. The following second-order polynomial Eqs. (28), (29) were obtained for both the responses.

$$R_{PP(THF)}=12.29-0.19X_1-0.28X_2-0.25X_3+0.002X_1X_2+0.003X_1X_3 +0.001X_2X_3+0.0006X_1^2+0.009X_2^2+0.003X_3^2 \quad (28)$$

$$R_{PP(water)}=6.27-0.04X_1+0.18X_2-0.21X_3-0.001X_1X_2+0.002X_1X_3 -0.0005X_1^2+0.002X_2^2+0.003X_3^2 \quad (29)$$

The predicted responses, developed by applying the above equations, were plotted with the experimental data (Fig. 7(j)-(k)). The adj. R^2 values for partial permeabilities of 1 and 2 were found to be as high as 0.9740 and 0.9757, respectively, which indicated the closeness of experimental and model predicted data. This authentication test also signified the rational applicability of the RSM generated quadratic model to explain the membrane intrinsic partial permeabilities. The optimum condition for attending the maximum THF permeance, via maintaining X_1, X_2, X_3 and partial permeability of water "in range" and partial permeability of THF "maximize", was X_1=35 °C, X_2=0.97 wt% and X_3=11.48 wt% (Fig. 7(g)-(i)). From Fig. 7(a), partial permeability of THF for SBRSEV0 was found to decrease from (6.14±0.17)×10^{-8} to (5.35±0.18)×10^{-8} Barrer by the rise in THF from 0.97 to 9.79 wt% at 35 °C, whereas water permeability was increased from (4.39±0.12)×10^{-8} to (5.16±0.17)×10^{-8} Barrer. From Fig. 7(g)-(i), the optimum partial permeabilities of THF and water were 4.64×10^{-8} and 2.94×10^{-8} Barrer, respectively. The variation of partial permeability as a function of feed composition could be better understood by comparing the plots of flux and fugacity (Fig. 4(e)). The used organoselective membranes showed higher partial permeabilities for THF than that of water in the entire concentration range studied. However, water permeability displayed hardly any deviation with increasing THF concentration for all the membranes. Indeed, both THF and water permeabilities were found to decrease with increasing amount of CBF in membranes, as observed by Singha et al. [8]. Partial permeability shows a direct relation to flux and inverse relation to vapour pressure difference between feed and permeate sides. The opposite trend of partial per-

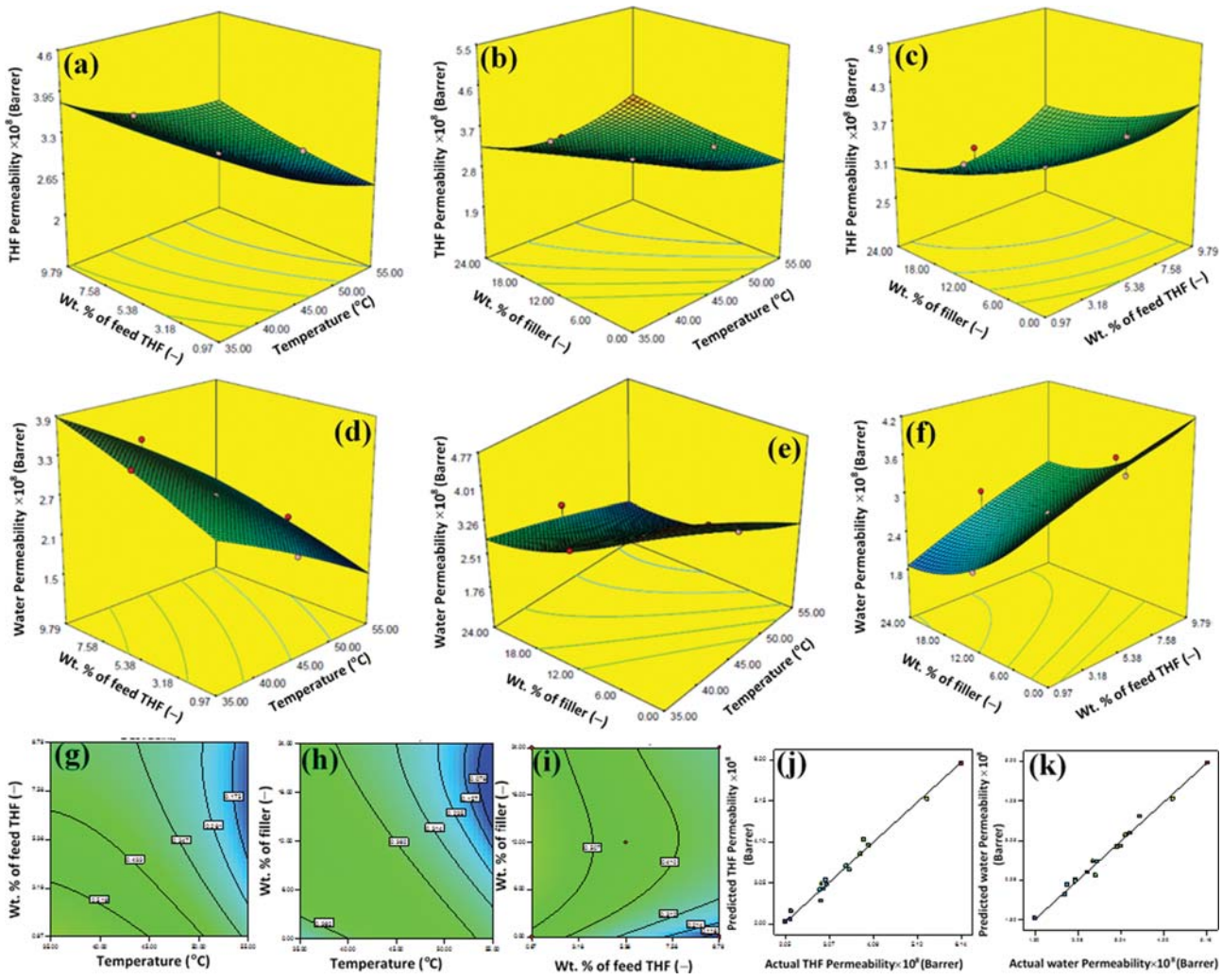

Fig. 7. The 3D response surface plots of PPs of THF/water vs. (a/d) wt% of feed THF/temperature, (b/e) wt% of filler/temperature, (c/f) wt% of filler/wt% of feed THF, (g)-(i) desirability plots and (j/k) validation plots of PPs of THF/water.

meability for THF in comparison to the flux with feed concentration might be explained in terms of variation of fugacity with feed concentration (Fig. 4(e)). It was evident that the rate of change in THF fugacity, i.e., denominator of Eq. (9a) and (9b) defining permeability, with THF in feed was much higher than that of partial flux, i.e., numerator of Eq. (9a), signifying the decrease in partial permeability of THF with increasing feed THF (Fig. 7(a) and (c)). The marginal variation of water permeability in the entire range was ascribed to the moderate variation of water fugacity and slight variation of partial flux. At higher feed concentration, substantial loosening of membrane matrix resulted in an increase in PP for THF. Similar results were also obtained for other rubber membranes [9]. The variation of partial permeabilities with temperature for used membranes is shown in Fig. 7(a), (b), (d) and (e). Although partial permeabilities of both THF and water decreased with rise in temperature, the rate of fall was relatively higher for THF. Again, with the increase in temperature, mobility of the permeants as well as segmental motion of the rubber chains were increased, which caused an increase in total flux (Fig. 6(a)-(b)). Meanwhile, the rate of increase in fugacity with temperature was found to be more rapid for THF (Fig. 4(e)). As partial permeability is inversely related to fugacity (Eq. (9a)), it falls more rapidly for THF instead of the increase in the THF flux. However, the prevalent voids of rubber membranes were filled by CBF, which allowed restricted permeation of both permeants. Thus, increase in water flux in the composite membranes with the rise in temperature was marginal. However, above 12 wt% of CBF loading, particle agglomeration (Fig. 3(d)) resulted in the enhancement of water flux and thus, restricted the decrease in water permeability.

13. Effect of Feed Concentration of THF on Diffusion Coefficients

The diffusion coefficients of THF were relatively higher than water in the entire concentration range studied (Fig. 4(f)). Indeed, diffusion coefficients of water were expected to be higher than THF, owing to smaller kinetic diameter of water, 0.265 nm, than THF, 0.585 nm [3]. However, the prevalence of the reverse trend could rationally be ascribed to the much higher THF sorption than water. In addition, the decrease in diffusion coefficients of both components with increasing CBF was correlated to the relative betterment of mechanical properties in composite membranes that re-

stricted the plasticization/permeation of both components, even at higher THF in feed. As favorable sorption and, hence, diffusion signified better separation, all the used SBRSEVs showed reasonable SF. The standard deviation within 2-4% of the mean value normally indicates fair reproducibility with high confidence limit. The diffusion coefficients of THF and water for SBRSEV0 membrane varied from $(16.62\pm0.47)\times10^{13}$ and $(2.80\pm0.20)\times10^{-13}$ to $(18.91\pm0.51)\times10^{-13}$ and $(6.27\pm0.42)\times10^{-13}$ m^2 s^{-1}, respectively, within 0.97-9.79 wt% THF at 35 °C (Fig. 4(f)).

14. Discussion of Mechanism

Mechanical properties and crosslink densities of vulcanized rubber membranes depend on the sulfidic bridge lengths, mono-/bi-/poly-sulfidic, which are controlled by the introduction of various A/S ratios. Meanwhile, EV (A/S=2.50-12.00), SEV (A/S=0.70-2.50) and CV (A/S=0.10-0.60) predominantly produce mono-, bi- and poly-sulfidic linkages, respectively. The RSM optimization showed SEV to result in the best balance between TS and EAB. Thus, in the present study, a rational mechanism of vulcanization and all the possible crosslinked products, along with the precursors, appeared during the process of crosslinking, has been reported (Scheme 2).

15. Accelerated Sulfur Vulcanization through Radical Path

The accelerated vulcanization process was initiated by interaction between ZDC and sulfur (S_8) to produce poly-sulfidic homologue of ZDC, which subsequently fragmented at higher temperature of 110 °C by homolytic cleavage of Zn-S bond, resulting in diethylthiocarbamoyl polysulfanyl radical (**1**). This radical can abstract allylic protons of SBR (**2**) to produce two types of allylic radicals (**3** and **4**). The polysulfanyl radical (**1**) can also undergo radical addition to the double bond of unreacted SBR, followed by rearrangement, to produce four polysulfanyl radicals (**5**, **6**, **7** and **8**). The allylic radicals (**3** and **4**) undergo radical combination to the polysulfanyl radicals (**5**, **6**, **7** and **8**), producing eight crosslinked SBR chains (**9a**, **b** to **12a**, **b**). These vulcanized products contain S_x as a crosslink unit, in which x varies from 1 to 8 to impart different extents of mono- (n=1), di- (n=2) and poly-sulfidic (n>2) crosslinks (Scheme 2).

16. DFT Analysis

The ground state energies and dipole moments of ZDC accelerated vulcanized products (9a/9b, 10a/10b, 11a/11b and 12a/12b) were determined (Scheme 3, 4 and S2) using LSDA of Gaussian 09 software and the basis set LanL2DZ. Indeed, the significant variations in stability, resulting from the successive increase in S-atom from 1 to 7, were comprehensively understood from the relative alterations in ground state energies and dipole moments (Table 10) [46]. As shown in Table 10, the changes in ground state energies were similar for 9a/9b, 10a/10b, 11a/11b and 12a/12b, in which the ground state energies were found to decrease with increasing S-atom due to the enhancement of distances between two

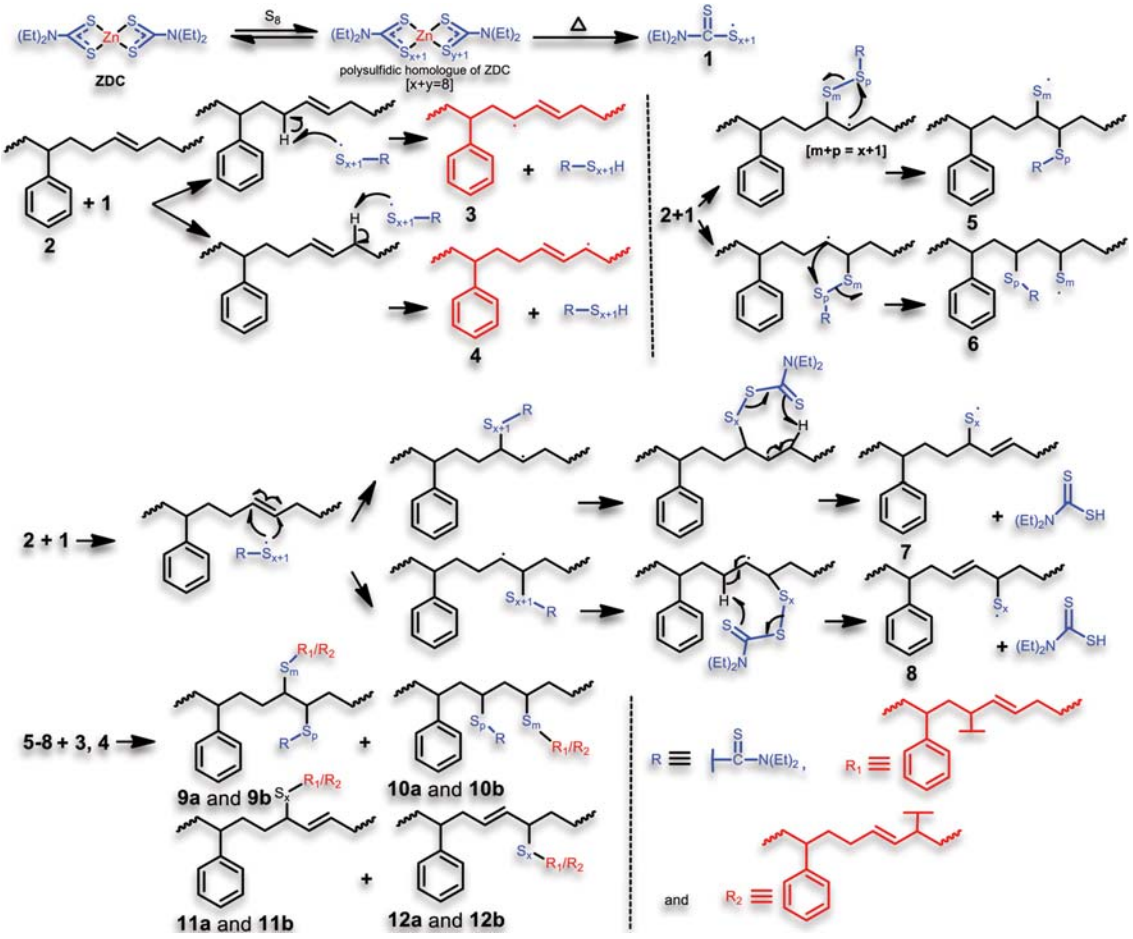

Scheme 2. Accelerated sulfur vulcanization of SBR through radical path.

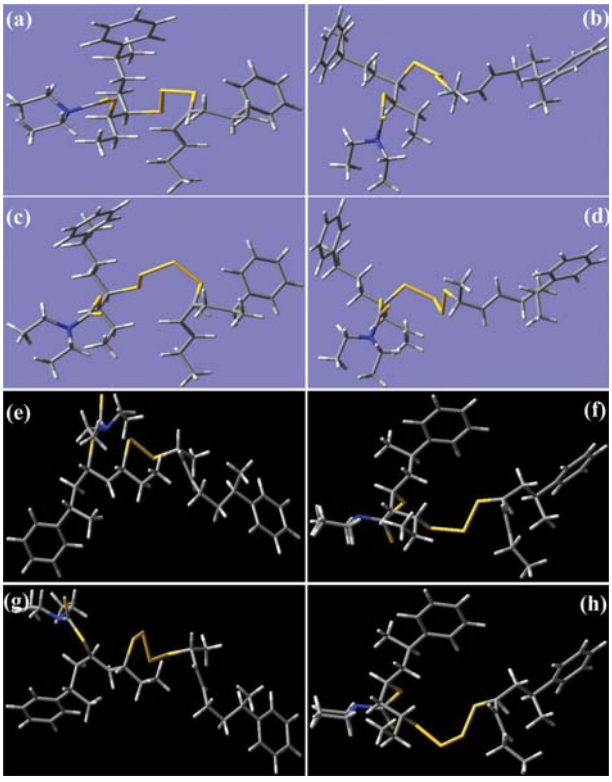

Scheme 3. DFT optimized structures of (a) 9a (S_p=1, S_m=3), (b) 9b (S_p=1, S_m=3), (c) 9a (S_p=1, S_m=4), (d) 9b (S_p=1, S_m=4), (e) 10a (S_p=1, S_m=3), (f) 10b (S_p=1, S_m=3), (g) 10a (S_p=1, S_m=4) and (h) 10b (S_p=1, S_m=4).

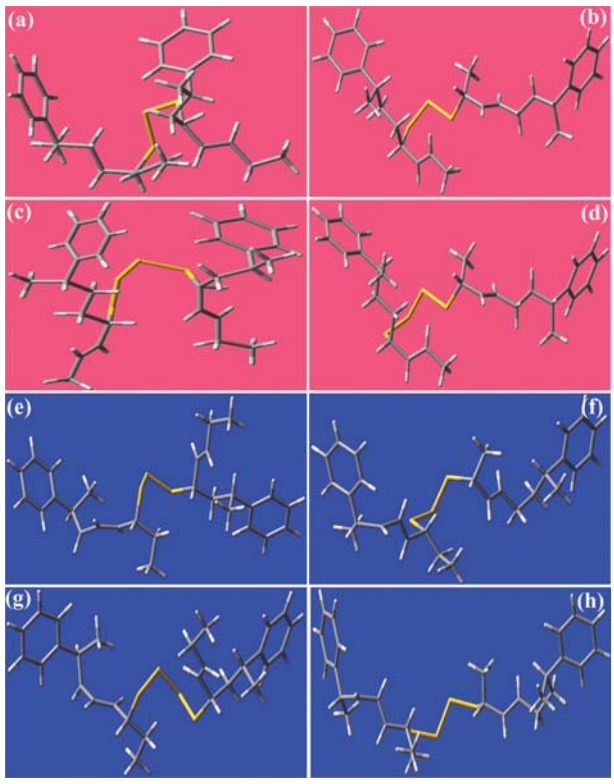

Scheme 4. DFT optimized structures of (a) 11a (S_x=3), (b) 11b (S_x=3), (c) 11a (S_x=4), (d) 11b (S_x=4), (e) 12a (S_x=3), (f) 12b (S_x=3), (g) 12a (S_x=4) and (h) 12b (S_x=4).

SBR matrices, whereas a random distribution of dipole moments was noted, depending on the relative changes in polarity of optimized structures. However, good balance of ground state energy and dipole moment for the several stable configurations indicated the attainment of diversified crosslinking and hence, the formation of crosslinked products of varied physicochemical properties.

17. Comparison of the Results Obtained with those Reported in Literature

Several synthetic membranes based on crosslinked copolymers,

Table 10. Variations of energies and dipole moments with the number of S atom(s)

(-) Energy (au)	Dipole moment (D)	Number of S atom(s)	(-) Energy (au)	Dipole moment (D)
9a		(p/m/S_p/S_m)	9b	
1363.888	4.620	1/1/S/S	1364.176	4.586
1374.335	3.559	1/2/S/S_2	1374.459	4.067
1384.300	4.968	1/3/S/S_3	1384.545	4.329
1394.677	6.011	1/4/S/S_4	1394.524	4.393
1404.712	6.708	1/5/S/S_5	1404.840	4.541
1414.868	7.311	1/6/S/S_6	1415.069	4.364
-	-	1/7/S/S_7	1425.238	6.578
10a		(p/m/S_p/S_m)	10b	
1364.017	4.488	1/1/S/S	1363.693	4.108
1374.420	4.932	1/2/S/S_2	1374.342	5.512
1384.593	4.797	1/3/S/S_3	1384.464	6.489
1394.696	5.019	1/4/S/S_4	1394.696	4.450
1404.890	6.020	1/5/S/S_5	1404.953	3.549
1414.980	5.730	1/6/S/S_6	1415.051	3.606
1425.177	7.258	1/7/S/S_7	1425.155	3.320

Table 10. Continued

(-) Energy (au)	Dipole moment (D)	Number of S atom(s)	(-) Energy (au)	Dipole moment (D)
11a		(x/S_x)	11b	
1093.514	2.330	1/S	1093.597	2.012
1103.635	3.520	$2/S_2$	1103.763	2.755
1113.627	3.932	$3/S_3$	1113.901	3.600
1123.923	5.418	$4/S_4$	1124.018	4.639
1134.132	6.109	$5/S_5$	1134.232	5.184
1144.279	6.888	$6/S_6$	1144.355	4.955
1154.434	7.451	$7/S_7$	1154.542	5.453
12a		(x/S_x)	12b	
1092.911	1.256	1/S	1092.917	1.612
1103.089	2.379	$2/S_2$	1103.081	2.457
1113.245	2.786	$3/S_3$	1113.246	3.858
1123.390	1.200	$4/S_4$	1123.397	4.628
1133.486	1.339	$5/S_5$	1133.551	4.649
1143.684	1.389	$6/S_6$	1143.684	4.821
1153.826	2.418	$7/S_7$	1153.827	4.643

Table 11. Comparison of THF removal performance of various pervaporation membranes from THF-water mixtures

Membranes used	Membrane thickness (mm)	Normalized flux (kg mm m^{-2} hr^{-1})/ Temperature (°C)/ THF in feed (wt%)	Separation factor (-)	Ref.
PP0[a]	50	0.56/30/0.90	125.00	[47]
F1[b]	50	0.95/30/0.90	84.00	[47]
UPVC[c]	30	0.21/30/0.90	125.00	[5]
PPVC-5[d]	30	0.63/30/0.90	62.88	[5]
PSTY[e]	30	0.49/30/0.90	71.97	[5]
Blend-5[f]	30	0.41/30/0.90	93.94	[5]
PTMSP-CL[g]	100	9.66/50/5.00	26.88	[48]
PAI-g-PDMS1[h]	100-200	39.30/50/6.99	75.40	[49]
PAI-g-PDMS3[h]	100-200	96.20/50/6.99	120.00	[49]
SBRSEV0[i]	50±0.55	3.18±0.08/35/0.97	170.353.74	TW*
SBRSEV8	50±0.55	2.78±0.06/35/0.97	177.40±3.90	TW
SBRSEV12	50±0.55	2.23±0.05/35/0.97	193.66±4.26	TW
SBRSEV24	50±0.55	1.84±0.04/35/0.97	208.33±4.59	TW

[a]Plasticized polyvinyl chloride membrane
[b]Polyvinyl chloride membrane containing 25 wt% of dioctyl phthalate and 1 wt% bentonite clay
[c]Unplasticized polyvinyl chloride membrane
[d]Plasticized polyvinyl chloride
[e]Polystyrene
[f]Blends of UPVC and PSTY
[g]Crosslinked poly[1-(trimethylsilyl)-1-propyne]
[h]Siloxane-grafted poly(amide-imide)
[i]Semi efficiently vulcanized styrene butadiene rubber membranes and *this work

graft copolymers and interpenetrating polymer network of varying thickness (i.e. 30-200 μm) have been reported in terms of normalized flux and SF at different feed concentrations of THF (0.9-6.99 wt%) and temperatures (30-50 °C). Instead of low THF concentration, low temperature and comparable thickness, the used membranes show excellent balance between SF and normalized flux using low cost synthetic rubber in an economically viable low energy green separation process (Table 11).

CONCLUSION

Physicochemically modified vulcanized-/composite SBR membranes of varying TS, EAB, modulus, physical-/chemical-crosslink density, solubility parameters and interaction parameters were used

in pervaporation of THF-water at different feed compositions and temperatures. The spectroscopic, thermal, mechanical, diffractometric microscopic and computational methods were employed for comprehensive analyses of crosslinking and variation in mechanical properties of membranes. State-I, state-II and state-III activity coefficients were determined by Flory-Huggins thermodynamics to ensure the coupling effect in sorption. The intrinsic properties, such as partial permeabilities and diffusion coefficients, were measured for unambiguous attainment of membrane property/performance variations with individual and interactive effects of X_1, X_2 and X_3 via three-stage RSM based optimization. The disappearance of olefinic backbone specific peaks at 132.90, 129.82, 127.52 and 116.07 ppm in SBRSEV0, along with the arrival of symbolic intense peak at 51.03 ppm for C-S crosslinking, implied the vulcanization through sulfur in SBRSEV0 network, as also ascertained from FTIR, TGA, DSC, XRD, SEM and DFT analyses. The formation of all possible crosslinked products from crosslink precursors, involving H-abstraction, radical addition, radical-radical coupling and sulfur-transfer, has also been incorporated to impart an unambiguous reaction mechanism, rationally supported by the computational analyses through DFT. The energies and dipole moments of different crosslinked networks produced during sulfur vulcanization were evaluated by DFT and the lowest energy configuration was identified. The unambiguous mechanistic studies of rubber vulcanization mechanism, comprising several pathways and intermediates, provide an innovative idea and impetus in the field of computational quantum mechanical modelling method to find the transition state(s), optimized structure(s) and activation energies through *ab initio* DFT studies. In terms of both NF (1.84± 0.04 kg μm m^{-2} h^{-1}) and SF (208.33±4.59) SBRSEV24 showed the optimum performance. These dimensionally stable membranes can be an attractive replacement of conventionally used polymeric membranes and effectively be introduced for the separation of any organic-water mixtures. This newly developed method of property-performance optimization can also be implemented for pervaporative separation of organics and dehydration by using peroxide or resol cured saturated and/or unsaturated synthetic rubber (e.g., NR, EPDM and PDMS) membranes, based on the closeness of SPs of both the membrane and the component to be separated. Finally, the novelty and versatility of the used membranes has been reflected by the attainment of significant physicochemical properties, performance characteristics and cost effective application prospects in green separation of organics from water.

ACKNOWLEDGEMENT

The corresponding author gratefully acknowledges Department of Science and Technology (DST), Government of India [YSS/2015/000886] and DST, Government of West Bengal [773(Sanc.)/ST/P/S&T/15G-2/2015] for providing financial assistance, and Department of Higher Education, Government of West Bengal for giving opportunity participating in inter-institutional collaboration with University of Calcutta. Mr. M. Mahapatra and Mr. M. Karmakar are grateful to University Grants Commission (UGC) (Sr. No.: 2061410291, Ref. No.: 22/06/2014 (i) EU-V and Roll No. 137632) and DST, Government of India (Ref. No.: IF160386), respectively, for providing fellowships.

SUPPORTING INFORMATION

Additional information as noted in the text. This information is available via the Internet at http://www.springer.com/chemistry/journal/11814.

REFERENCES

1. M. Karmakar, M. Mahapatra and N. R. Singha, *Korean J. Chem. Eng.*, **34**, 1416 (2017).
2. N. R. Singha and S. K. Ray, *J. Appl. Polym. Sci.*, **124**, E99 (2012).
3. N. R. Singha, T. K. Parya and S. K. Ray, *J. Membr. Sci.*, **340**, 35 (2009).
4. S. Roy and N. R. Singha, *Membranes*, **7** (2017), DOI:10.3390/membranes7030053.
5. N. R. Singha, S. Kar, S. Ray and S. K. Ray, *Chem. Eng. Process.*, **48**, 1020 (2009).
6. N. R. Singha, S. B. Kuila, P. Das and S. K. Ray, *Chem. Eng. Process.*, **48**, 1560 (2009).
7. N. R. Singha, S. Ray, S. K. Ray and B. B. Konar, *J. Appl. Polym. Sci.*, **121**, 1330 (2011).
8. N. R. Singha, P. Das and S. K. Ray, *J. Ind. Eng. Chem.*, **19**, 2034 (2013).
9. M. Mahapatra, M. Karmakar, B. Mondal and N. R. Singha, *RSC Adv.*, **6**, 69387 (2016).
10. M. D. Kurkuri, J. N. Nayak, M. I. Aralaguppi, B. V. K. Naidu and T. M. Aminabhavi, *J. Appl. Polym. Sci.*, **98**, 178 (2005).
11. M. Khayet, C. Cojocaru and G. Zakrzewska-Trznadel, *J. Membr. Sci.*, **321**, 272 (2008).
12. M. Catarino, A. Ferreira and A. Mendes, *J. Membr. Sci.*, **341**, 51 (2009).
13. V. García, J. L. Aguirre, E. Pongrácz, P. Perämäki and R. L. Keiski, *J. Membr. Sci.*, **338**, 111 (2009).
14. S. B. Kuila, S. K. Ray, P. Das and N. R. Singha, *Chem. Eng. Process.*, **50**, 391 (2011).
15. P. Das, S. K. Ray, S. B. Kuila, H. S. Samanta and N. R. Singha, *Sep. Purif. Technol.*, **81**, 159 (2011).
16. N. R. Singha, A. Dutta, M. Mahapatra, M. Karmakar, H. Mondal, P. K. Chattopadhyay and D. K. Maiti, *ACS Omega*, **3**, 472 (2018).
17. N. R. Singha, M. Mahapatra, M. Karmakar, H. Mondal, A. Dutta, M. Deb, M. Mitra, C. Roy, P. K. Chattopadhyay and D. K. Maiti, *ACS Omega*, **3**, 4163 (2018).
18. H. S. Samanta, S. K. Ray, P. Das and N. R. Singha, *J. Chem. Technol. Biot.*, **87**, 608 (2012).
19. N. Valentínyi, E. Cséfalvay and P. Mizsey, *Chem. Eng. Res. Des.*, **91**, 174 (2013).
20. N. R. Singha, S. Kar and S. K. Ray, *Sep. Sci. Technol.*, **44**, 422 (2009).
21. S. Ray, N. R. Singha and S. K. Ray, *Chem. Eng. J.*, **149**, 153 (2009).
22. N. R. Singha and S. K. Ray, *Sep. Sci. Technol.*, **45**, 2298 (2010).
23. G. Socrates, Infrared and Raman Characteristic Group Frequencies: Tables and Charts, Wiley, New York (2001).
24. A. S. Z. Naseri and A. J. Arani, *Radiat. Phys. Chem.*, **115**, 68 (2015).
25. S. Gunasekaran, R. K. Natarajan and A. Kala, *Spectrochim. Acta A*, **68**, 323 (2007).

26. X. Liu, S. Zhao, X. Zhang, X. Li and Y. Bai, *Polymer*, **55**, 1964 (2014).
27. V. Pouchaname, A. Tinabaye, R. Madivanane and Dr. Renukadevi, *IRACST-Engineering Science and Technology: An International Journal*, **2**, 752 (2012).
28. M. J. Fernandez-Berridi, N. Gonzalez, A. Mugica and C. Bernicot, *Thermochim. Acta*, **444**, 65 (2006).
29. Y. S. Lee, W. Lee, S. Cho, I. Kim and C. Ha, *J. Anal. Appl. Pyrolysis*, **78**, 85 (2007).
30. H. Li, H. Kang, W. Zhang, S. Zhang and J. Li, *Int. J. Adhes. Adhes.*, **66**, 59 (2016).
31. G. Mertz, F. Hassouna, V. Toniazzo, A. Dahoun and D. Ruch, *J. Eng. Mater. Technol.*, **134**, 0109031 (2012).
32. P. A. Ajibade and B. C. Ejelonu, *Spectrochim. Acta A*, **113**, 408 (2013).
33. L. Pellicioli, S. K. Mowdood, F. Negroni, D. D. Parker and J. L. Koenig, *Rubber Chem. Technol.*, **75**, 65 (2002).
34. N. R. Singha, M. Karmakar, M. Mahapatra, H. Mondal, A. Dutta, C. Roy and P. K. Chattopadhyay, *Polym. Chem.*, **8**, 3211 (2017).
35. N. R. Singha, S. Kar and S. K. Ray, *Sep. Sci. Technol.*, **44**, 1970 (2009).
36. A. Arockiasamy, H. Toghiani, D. Oglesby, M. F. Horstemeyer, J. L. Bouvard and R. L. King, *J. Therm. Anal. Calorim.*, **111**, 535 (2013).
37. S. J. Lue, W. W. Chen and S. F. Wang, *Sep. Sci. Technol.*, **44**, 3412 (2009).
38. P. Li, L. Yin, G. Song, J. Sun, L. Wang and H. Wang, *Appl. Clay Sci.*, **40**, 38 (2008).
39. S. Ray and S. K. Ray, *J. Membr. Sci.*, **270**, 132 (2006).
40. N. R. Singha, M. Karmakar, M. Mahapatra, H. Mondal, A. Dutta, M. Deb, M. Mitra, C. Roy and P. K. Chattopadhyay, *J. Mater. Chem. A*, **6**, 8078 (2018).
41. P. K. Chattopadhyay, N. C. Das and S. Chattopadhyay, *Compos. Part A: Appl. Sci. Manuf.*, **42**, 1049 (2011).
42. R. Guo, C. Hu, B. Li and Z. Jiang, *J. Membr. Sci.*, **289**, 191 (2007).
43. M. Karmakar, M. Mahapatra, A. Dutta, P. K. Chattopadhyay and N. R. Singha, *Int. J. Biol. Macromol.*, **102**, 438 (2017).
44. M. Mahapatra, M. Karmakar, A. Dutta, H. Mondal, J. S. D. Roy, P. K. Chattopadhyay and N. R. Singha, *J. Environ. Chem. Eng.*, **6**, 289 (2018).
45. R. V. Kumar, I. G. Moorthy and G. Pugazhenthi, *RSC Adv.*, **5**, 87645 (2015).
46. N. R. Singha, M. Mahapatra, M. Karmakar, A. Dutta, H. Mondal and P. K. Chattopadhyay, *Polym. Chem.*, **8**, 6750 (2017).
47. P. Das and S. K. Ray, *J. Ind. Eng. Chem.*, **34**, 321 (2016).
48. S. Claes, P. Vandezande, S. Mullens, P. Adriaensens, R. Peeters, F. H. J. Maurer and M. K. V. Bael, *J. Membr. Sci.*, **389**, 459 (2012).
49. Y. Nagase, T. Ando and C. M. Yun, *React. Funct. Polym.*, **67**, 1252 (2007).

Supporting Information

Fabrication of composite membranes for pervaporation of tetrahydrofuran-water: Optimization of intrinsic property by response surface methodology and studies on vulcanization mechanism by density functional theory

Manas Mahapatra, Mrinmoy Karmakar, Arnab Dutta, and Nayan Ranjan Singha[†]

Advanced Polymer Laboratory, Department of Polymer Science and Technology,
Government College of Engineering and Leather Technology (Post-Graduate),
Maulana Abul Kalam Azad University of Technology, Salt Lake, Kolkata - 700106, West Bengal, India
(*Received 31 January 2018 • accepted 13 June 2018*)

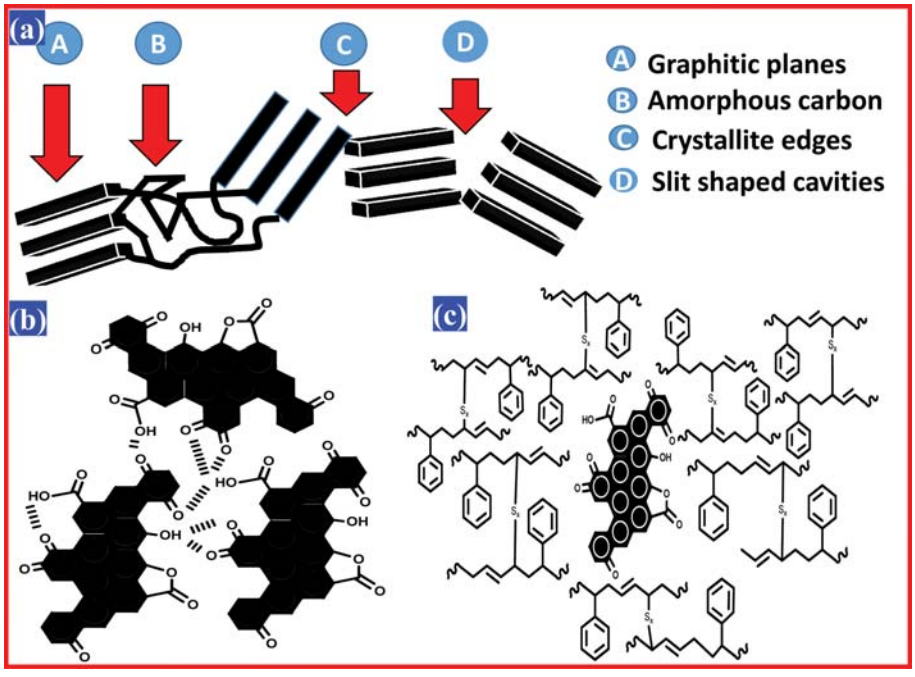

Scheme S1. (a) Attribution of adsorption sites, (b) agglomeration of CB particles in rubber matrix via physical/chemical interactions and (c) schematic representation of interactions between CBF and rubber chains.

Entry		S_m, S_p	
	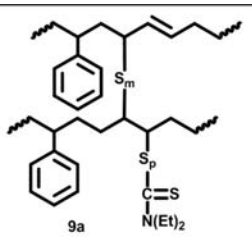 9a		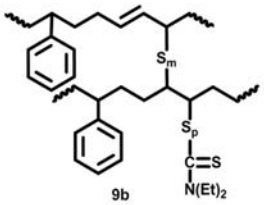 9b
	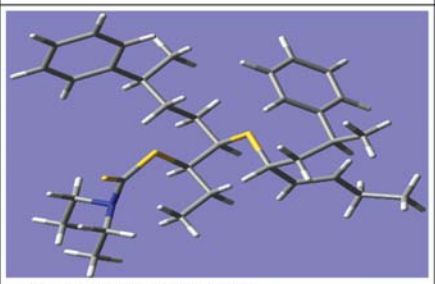 E (au) = -1363.88805825 μ (D) = 4.6200	S_p = 1 S_m= 1	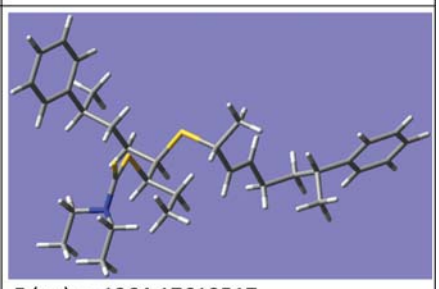 E (au) = -1364.17619517 μ (D) = 4.5857
	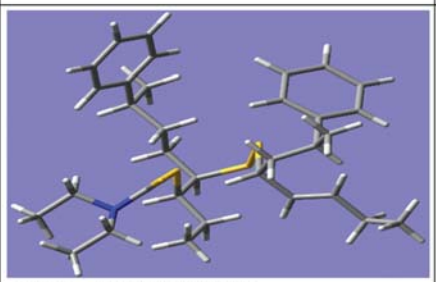 E (au) = -1374.33528446 μ (D) = 3.5591	S_p= 1 S_m = 2	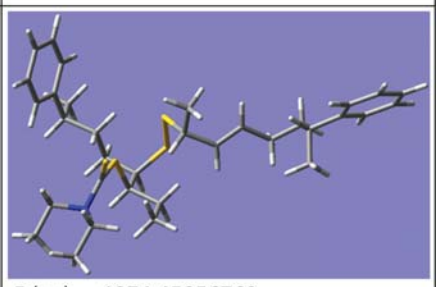 E (au) = -1374.45856769 μ (D) = 4.0670
	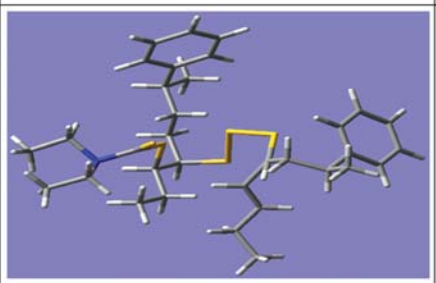 E (au) = -1384.30033530 μ (D) = 4.9677	S_p= 1 S_m = 3	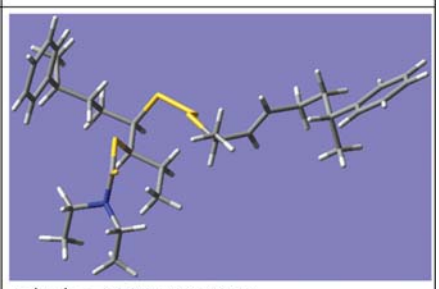 E (au) = -1384.54494647 μ (D) = 4.3293

Scheme S2. DFT optimized structures of 9a, 9b, 10a, 10b, 11a, 11b, 12a and 12b.

	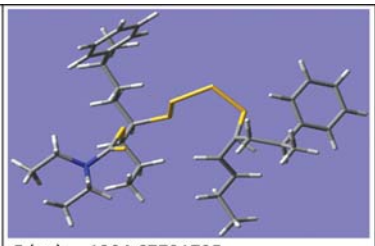 E (au) = -1394.67731735 μ (D) = 6.0112	S_p= 1 S_m = 4	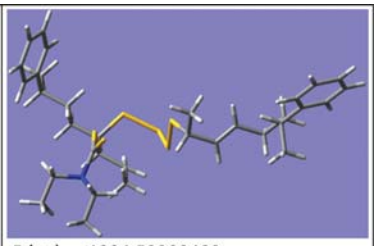 E (au) = -1394.52393492 μ (D) = 4.3935
	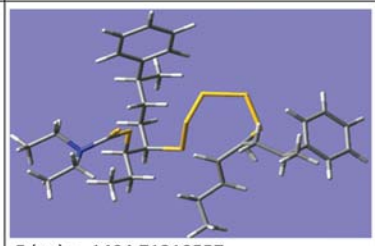 E (au) = -1404.71210557 μ (D) = 6.7082	S_p=1 S_m = 5	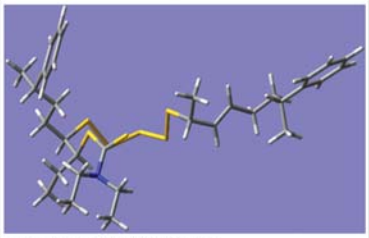 E (au) = -1404.83984741 μ (D) = 4.5410
	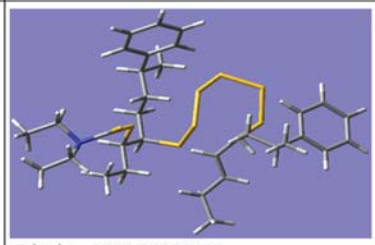 E (au) = -1414.86838461 μ (D) = 7.3114	S_p=1 S_m = 6	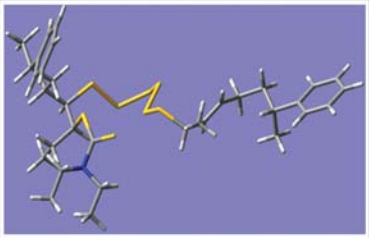 E (au) = -1415.06875225 μ (D) = 4.3638
		S_p=1 S_m = 7	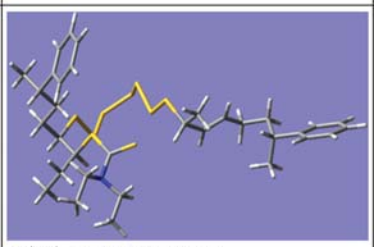 E (au) = -1425.23766732 μ (D) = 6.5779

Scheme S2. Continued.

Entry	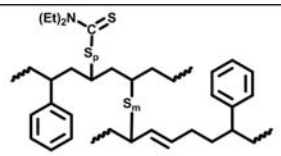 10b	S_p, S_m	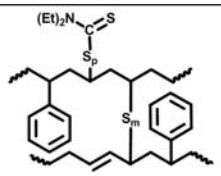 10a
	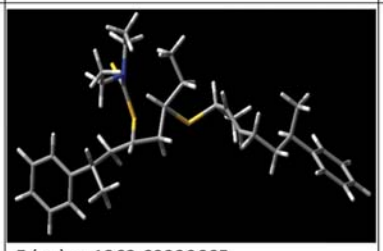 E (au) = -1363.69330665 μ (D) = 4.1083	S_p = 1 S_m = 1	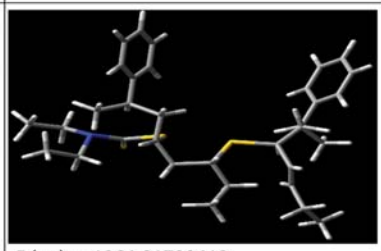 E (au) = -1364.01729419 μ (D) = 4.4885
	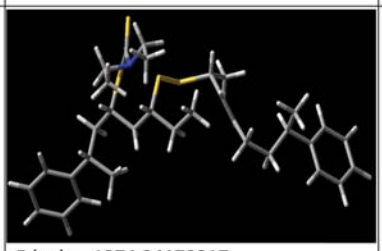 E (au) = -1374.34179217 μ (D) = 5.5119	S_p = 1 S_m = 2	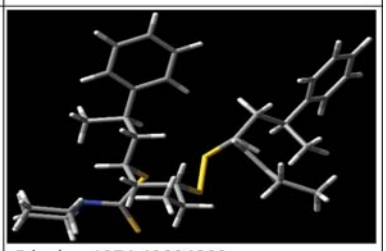 E (au) = -1374.42024802 μ (D) = 4.9326
	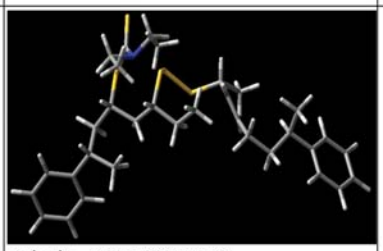 E (au) = -1384.46357159 μ (D) = 6.4889	S_p = 1 S_m = 3	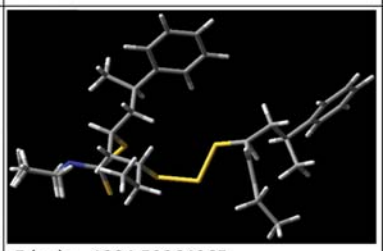 E (au) = -1384.59264965 μ (D) = 4.7968

Scheme S2. Continued.

	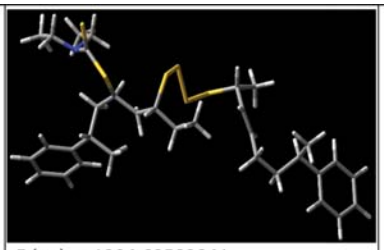 E (au) = -1394.69582941 μ (D) = 4.4506	$S_p = 1$ $S_m = 4$	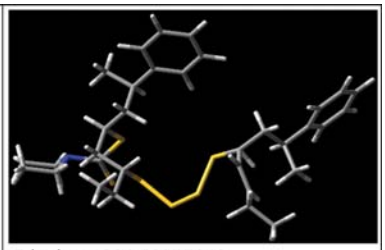 E (au) = -1394.69575942 μ (D) = 5.0190
	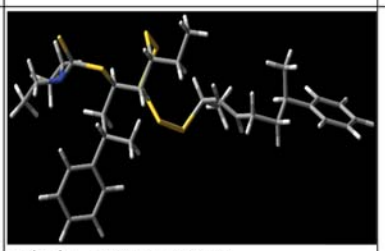 E (au) = -1404.95349470 μ (D) = 3.5495	$S_p = 1$ $S_m = 5$	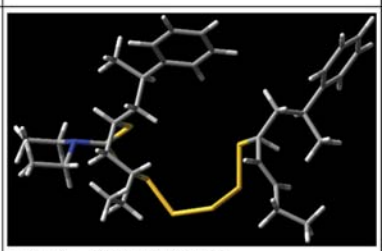 E (au) = -1404.89000304 μ (D) = 6.0199
	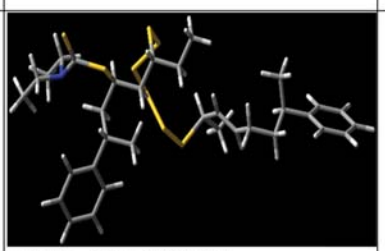 E (au) = -1415.05090357 μ (D) = 3.6060	$S_p = 1$ $S_m = 6$	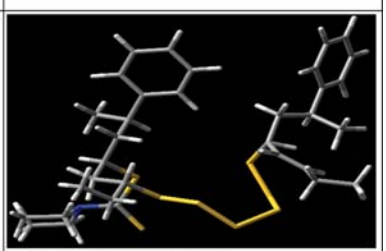 E (au) = -1414.97984553 μ (D) = 5.7296
	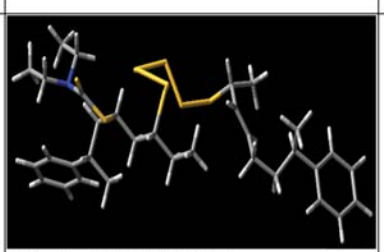 E (au) = -1425.15465937 μ (D) = 3.3205	$S_p = 1$ $S_m = 7$	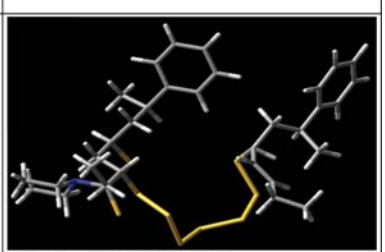 E (au) = -1425.17660095 μ (D) = 7.2575

Scheme S2. Continued.

Entry	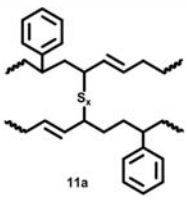 11a		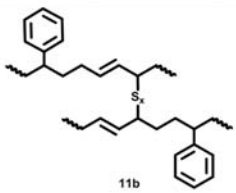 11b
	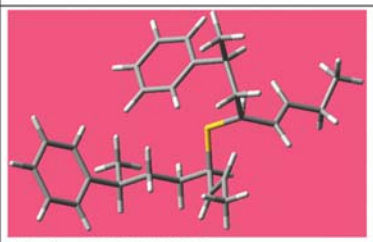 E (au): -1093.51456140 μ (D): 2.3295	S_x = 1	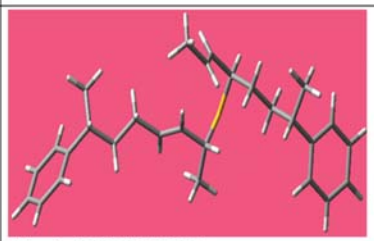 E (au): -1093.59772328 μ (D): 2.0123
	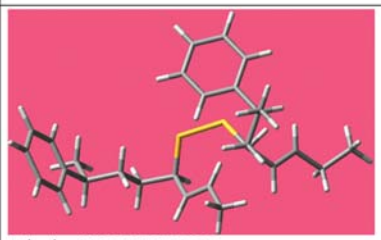 E (au): -1103.63538862 μ (D): 3.5194	S_x = 2	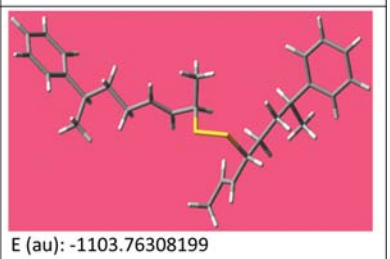 E (au): -1103.76308199 μ (D): 2.7547
	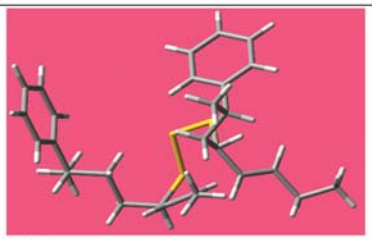 E (au): -1113.62732107 μ (D): 3.9325	S_x = 3	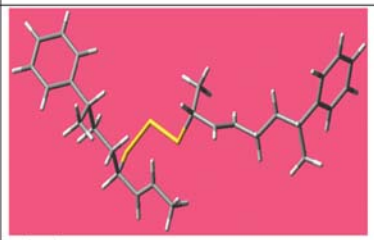 E (au): -1113.90125849 μ (D): 3.6002

Scheme S2. Continued.

	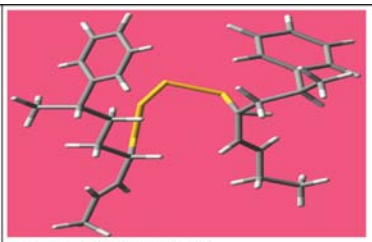 E (au): -1123.92362621 μ (D): 5.4176	$S_x = 4$	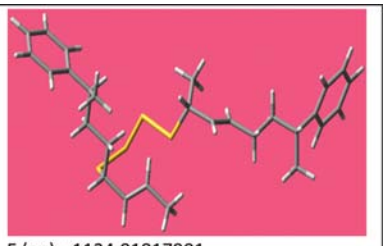 E (au): -1124.01817901 μ (D): 4.6395
	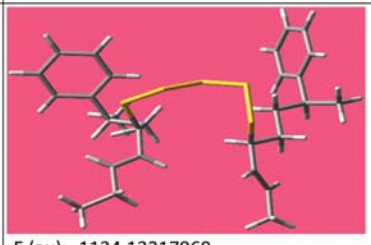 E (au): -1134.13217969 μ (D): 6.1091	$S_x = 5$	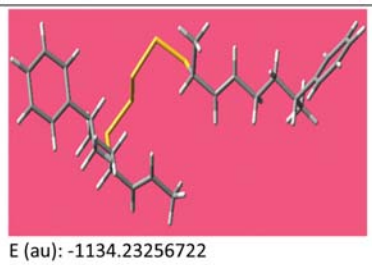 E (au): -1134.23256722 μ (D): 5.1838
	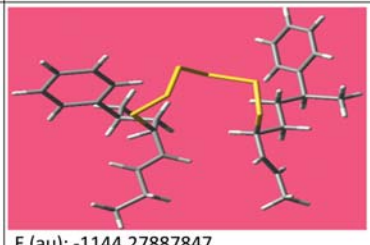 E (au): -1144.27887847 μ (D): 6.8883	$S_x = 6$	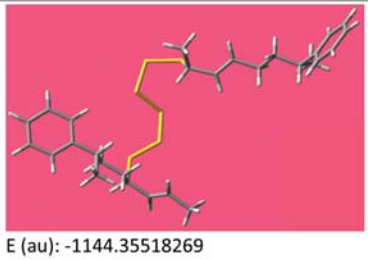 E (au): -1144.35518269 μ (D): 4.9546
	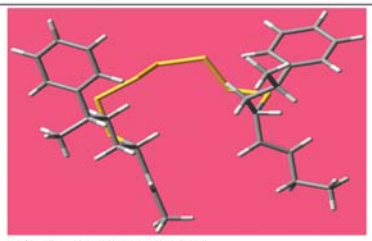 E (au): -1154.43414327 μ (D): 7.4511	$S_x = 7$	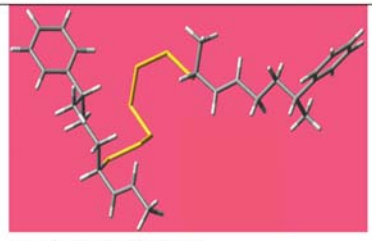 E (au): -1154.54232161 μ (D): 5.4535

Scheme S2. Continued.

Entry	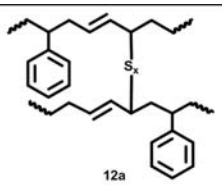 12a	S_x	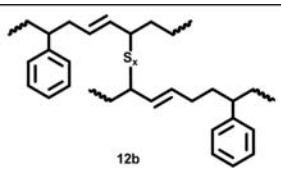 12b
	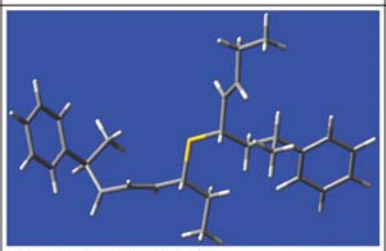 E (au): -1092.91172224 μ (D): 1.2560	S_x = 1	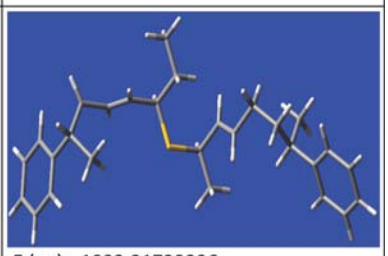 E (au): -1092.91722236 μ (D): 1.6121
	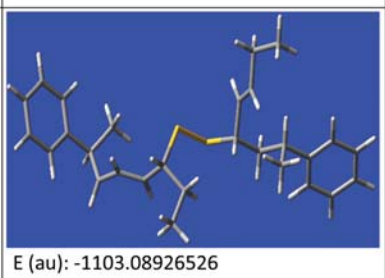 E (au): -1103.08926526 μ (D): 2.3791	S_x = 2	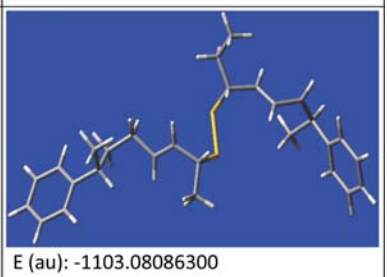 E (au): -1103.08086300 μ (D): 2.4569
	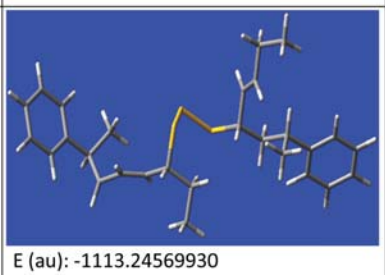 E (au): -1113.24569930 μ (D): 2.7863	S_x = 3	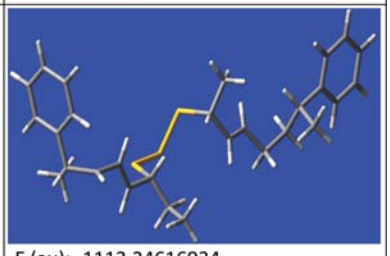 E (au): -1113.24616934 μ (D): 3.8576

Scheme S2. Continued.

	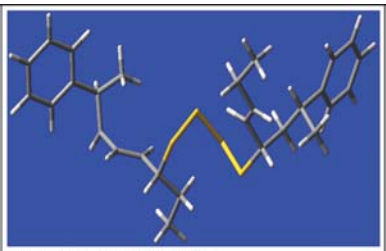 E (au): -1123.39033239 μ (D): 1.2006	S_x = 4	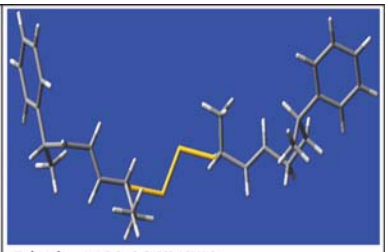 E (au): -1123.39671758 μ (D): 4.6277
	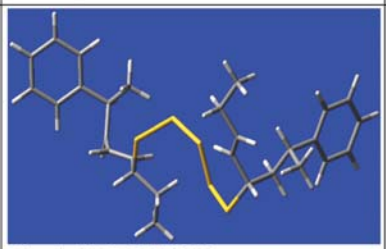 E (au):-1133.48651454 μ (D): 1.3388	S_x = 5	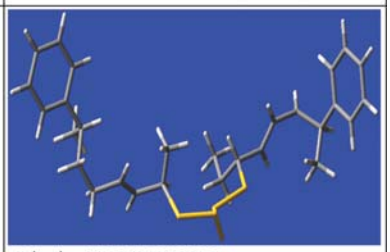 E (au): -1133.55079072 μ (D): 4.6486
	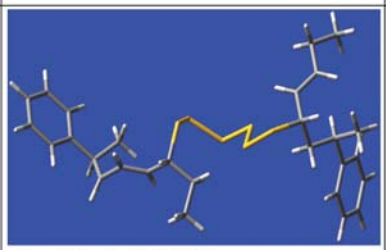 E (au): -1143.68405769 μ (D): 1.3898	S_x = 6	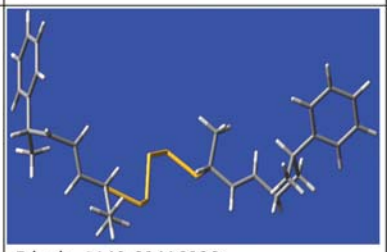 E (au): -1143.68416938 μ (D): 4.8208
	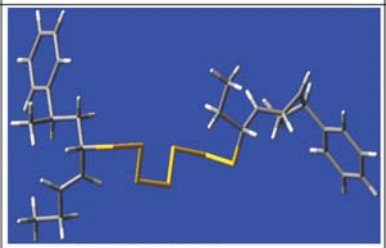 E (au): -1153.82616975 μ (D): 2.4180	S_x = 7	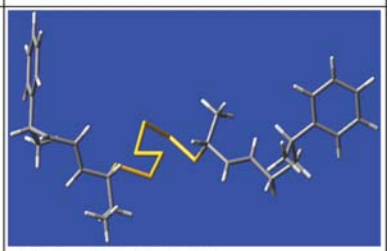 E (au): -1153.82705600 μ (D): 4.6428

Scheme S2. Continued.